A&A 389, 993–1014 (2002)
DOI: 10.1051/0004-6361:20020543

Astronomy & Astrophysics

Interstellar CN toward CH^+-forming regions

R. Gredel[1], G. Pineau des Forêts[2], and S. R. Federman[3]

[1] Max-Planck Institut für Astronomie, Königstuhl 17, 69117 Heidelberg, Germany
e-mail: gredel@caha.es
[2] IAS, Université de Paris-Sud, Bât. 121, 92405 Orsay Cedex, France
e-mail: forets@obspm.fr
[3] Department of Physics and Astronomy, University of Toledo, Toledo, OH 43606, USA
e-mail: sfederm@uoft02.utoledo.edu

Received 22 January 2002 / Accepted 8 April 2002

Abstract. Measurements on interstellar CN absorption are presented for stars in three southern OB associations, NGC 2439, Vela OB1, and Cen OB1. CN is detected in 21 out of 31 stars observed. The doublet ratio for the $R(1)$ and $P(1)$ lines of the (0, 0) band of the B $^2\Sigma^+$–X $^2\Sigma^+$ violet system and a comparison of violet system data with measurements of the (1, 0) and (2, 0) bands of the A $^2\Pi$–X $^2\Sigma^+$ red system are used to derive Doppler parameters and total column densities. Inferred CN column densities vary by more than an order of magnitude for lines of sight with similar CH column densities. Observations of the (0, 0) band of the CH B $^2\Sigma^-$–X $^2\Pi$ system are used to revise previously published CH column densities toward the lines of sight studied in CN. Together with earlier results on CH, CH^+, and C_2, the CN data presented here provide a homogeneous set of column densities and radial velocities of diatomic molecules in three individual translucent clouds. We use these data to study CN production via chemical models. Gas densities are inferred from models based on production via CH and C_2 in cool gas. Most sightlines in our sample test densities typical for diffuse molecular gas (a few hundred cm^{-3}) when the ultraviolet flux permeating the gas is between 1 and 5 times the average interstellar flux. A few lines of sight indicate that CN is produced under dark cloud conditions because relatively large densities are obtained or because this simple chemical scheme is unable to reproduce the observed CN columns. Low densities are indicated for directions with upper limits on CN. We add an ad hoc component of a number of low-velocity ($<$10 km s^{-1}) criss-crossing MHD shocks to explain observed column densities of interstellar CH^+. These shocks also produce about 10 to 30% of the total CH column along the line of sight.

Key words. ISM: general – ISM: abundances – ISM: clouds – ISM: molecules

1. Introduction

In diffuse molecular gas, CN is a probe of relatively dense regions (e.g., Joseph et al. 1986). A survey of 15 lines of sight with known molecular hydrogen abundances was used to identify the basic reactions which are responsible for the formation of CN in diffuse clouds (Federman et al. 1984; Federman & Lambert 1988). For total molecular hydrogen columns of $N(H_2) \leq 10^{21}$ cm^{-2}, the column density of CN is found to correlate with that of H_2, with $\log N(CN) \approx 3 \log N(H_2)$ (Federman et al. 1984). Toward more reddened lines of sight, the correlation seems to break down. Two studies presented by van Dishoeck & Black (1989) and Gredel et al. (1991) of some 27 lines of sight with visual extinctions up to 5 mag showed that the CN column densities may vary by more than an order of magnitude for lines of sight where the CH column densities are similar. From a comparison of their model calculations with the observations, van Dishoeck & Black (1989) suggested that the large differences in the CN/CH column densities may arise from variations in the intensity of the UV radiation field at $\lambda < 1000$ Å. More recently, Federman et al. (1994) pointed out that the chemistry of CN, and that of C_2, is affected by chemical transitions, which take place at grain optical depths $\tau_{UV} > 3$ where neutral-neutral reactions of N with CH and C_2 dominate CN production channels, and at $\tau_{UV} \geq 4.5$ where photodissociation of CN ceases to be important. The rate equations for C_2 and CN developed by Federman et al. (1994) were used to extract physical conditions in

Send offprint requests to: R. Gredel,
e-mail: gredel@mpia.de

photodissociation regions toward stars illuminating reflection nebulae (Federman et al. 1997a; Knauth et al. 2001) and to study density variations over subparsec scales in diffuse molecular gas (Pan et al. 2001). Limits on CN abundances also place constraints on the amount of CH produced during CH^+ synthesis (Federman et al. 1997b; Zsargó 2000). This highlights the different regions probed by CN and CH^+ absorption. A goal of the present study is to examine this correspondence for gas toward three southern associations.

A very different aspect of interstellar CN is its use to determine the cosmic microwave background radiation temperature, $T_{\rm CMB}$. Very successfully, high signal to noise observations of optical absorption lines have been used to derive a value of $T_{\rm CMB} = 2.73$ K (e.g., Roth & Meyer 1995, and references therein), which agrees remarkably well with the value of $T_{\rm CMB} = 2.728$ K determined by COBE toward the Galactic North Pole (Fixsen et al. 1997). Collisional impact excitation by electrons may, however, increase the CN excitation temperature above $T_{\rm CMB}$ (Black & van Dishoeck 1991) in clouds where the fractional ionisation is high. The CN rotational excitation temperature which is inferred from the measurements may also be used to judge whether the inferred CN column densities are reliable or not.

The focus of the present work is to complement previously reported observations of CH^+, CH, and C_2 toward the three southern OB associations NGC 2439, Vela OB1, and Cen OB1 (Gredel 1997, 1999). The study of molecular abundances toward members of a given association gives some confidence that variations in the column densities arise from variations in the physical and chemical conditions in spatially coherent structures or clouds. In particular, the variation in the molecular abundances with visual extinction of the background stars may be used to study the dependence of the molecular material on optical depth of a cloud. With the addition of CN presented below, we provide a homogeneous set of column densities and radial velocities of diatomic molecules in three translucent clouds. Our observations focused on the CN absorption lines which arise from the (0, 0) band of the B $^2\Sigma^+$–X $^2\Sigma^+$ violet system. Additional data on the (1, 0) and (2, 0) bands of the CN A $^2\Pi$–X $^2\Sigma^+$ red system are used to obtain saturation corrections. The observations are discussed in Sect. 2. The methods used to estimate the CN Doppler parameters, b(CN), and the saturation corrections are described in Sect. 3.1. Our spectra of the CN violet system cover absorption lines which arise from the (0, 0) band of the CH B $^2\Sigma^-$–X $^2\Pi$ system as well. The new CH data are used to verify the previously inferred CH column densities (Gredel 1997, hereafter Paper I) and to check whether the saturation corrections which were applied to derive column densities are reasonable or not. The new CH data are presented in Sects. 2.3 and 3.2. A comparison of the radial velocities of CN, CH^+, CH, and C_2 is given in Sect. 4.1. Derived CN column densities are compared with general predictions from theoretical models and are used to infer gas densities (Sect. 4.2). We aim to explain the observed CH^+ column densities by introducing an ad hoc component of some 10–50 criss-crossing MHD shocks per line of sight (Sect. 4.3).

2. Observations and data reduction

2.1. The (0, 0) band of the B $^2\Sigma^+$–X $^2\Sigma^+$ CN violet system

Absorption from the $R(0)$, $R(1)$, and $P(1)$ lines of the (0, 0) band of the CN B $^2\Sigma^+$–X $^2\Sigma^+$ violet system was sought toward early type stars in the NGC 2439, Vela OB1, and Cen OB1 associations, using the 1.4 m Coudé Auxiliary Telescope (CAT) on La Silla. The observations were obtained during the nights of April 6–11, 1997 under good atmospheric conditions. The Coudé Echelle Spectrograph (CES) was used at a spectral resolving power of $R = \lambda/\Delta\lambda = 60\,000$. Total exposure times range from 0.5–2 hours and were set to reach a signal-to-noise ratio in the stellar continuum of $S/N \geq 100$ in general. The observations were reduced following standard procedures – see Gredel et al. 1991 for details. The $R(0)$, $R(1)$, and $P(1)$ lines are unresolved blends of two or three spin-rotation components, $[R_1(0) + {}^RQ_{12}(0)]$, $[R_1(1) + R_2(1) + {}^RQ_{12}(1)]$, and $[P_1(1) + {}^PQ_{12}(1)]$, with effective rest wavelengths of 3874.602 Å, 3873.994 Å, and 3875.759 Å, respectively (Prasad et al. 1992). In the limit of unsaturated lines, the equivalent widths W_λ are converted into column density N_∞ using $N_\infty = 1.13 \times 10^{20}\, W_\lambda/\lambda^2 f_{J'J''}$, where N_∞ is in units of cm^{-2} and W_λ and λ are both in Å. Line oscillator strengths $f_{J'J''}$ are factorised into $f_{J'J''} = p_{J'J''} f_{00}$, with values of $p_{J'J''}$ of 1.0, 0.667, and 0.333, for the $R(0)$, $R(1)$, and $P(1)$ line blends, respectively (Federman et al. 1984). We adopt the theoretical band oscillator strengths of $f_{00} = 0.0342$ of Bauschlicher et al. (1988).

The final spectra for stars in NGC 2439, Vela OB1, and Cen OB1 are shown in Figs. 1–3, respectively. All spectra are normalised to a continuum level of 1 and are in a heliocentric reference frame. CN absorption lines are detected in all observed stars in NGC 2439, in 7 out of 10 stars in the Vela OB1 Association, and in 8 out of 10 stars in Cen OB1. Note that HD 78344 is considered a probable member of Vela OB1 (Reed 2000). Toward HD 110639, HD 113422, and HD 114213, the CN absorption occurs in 2 well resolved velocity components. Toward HD 61827, the CN absorption lines are partially resolved into two velocity components. Additional spectra not shown here were taken of HD 54662 in CMa OB1, and of HD 111904, HD 111973, HD 111990, and CPD−59°4551 in NGC 4755; CN is not detected toward any of these stars and upper limits are $N(\mathrm{CN}) < 5 \times 10^{11}$ cm^{-2}.

The measurements are summarised in Tables 1 and 2, with the stellar ID, the line designation, the heliocentric wavelength $\lambda_{\rm hel}$ in Å, the corresponding heliocentric velocity $V_{\rm hel}$ in km s^{-1}, the measured equivalent width W_λ in mÅ, and the corresponding column density $N_\infty(N'')$ inferred in the limit of unsaturated lines in Cols. 1–6,

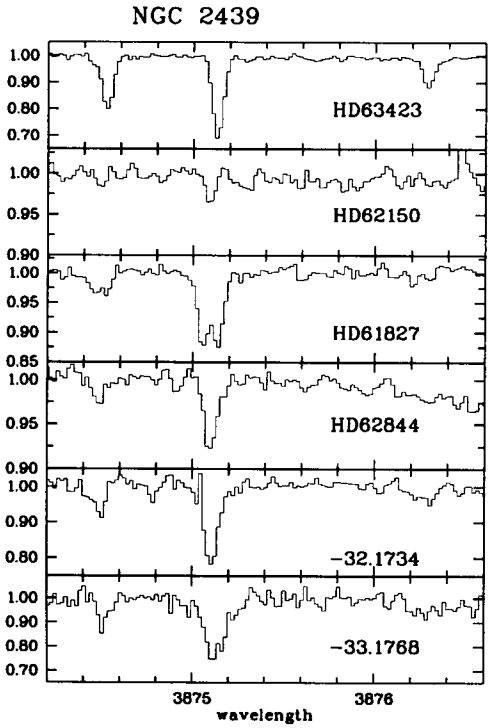

Fig. 1. $R(0)$, $R(1)$, and $P(1)$ absorption lines of the (0, 0) band of the CN B $^2\Sigma^+$–X $^2\Sigma^+$ violet system toward various stars in the NGC 2439 association.

respectively. Measurement uncertainties in the equivalent widths are dominated by the uncertainties in the placement of the local stellar continuum rather than by the noise in the stellar continuum. The uncertainties in W_λ and the resulting uncertainties in the inferred column densities are given in parentheses in Cols. 5 and 6, respectively. The heliocentric velocities $\overline{V_{\rm hel}}$ listed in Col. 7 are averages, with the oscillator strengths of the corresponding absorption lines used as the weighting factor.

2.2. The (1, 0) and (2, 0) bands of the CN $A\,^2\Pi$–$X\,^2\Sigma^+$ red system

Interstellar absorption lines in the (1,0) and (2,0) bands of the A $^2\Pi$–X $^2\Sigma^+$ CN red system are detected in the echelle spectra of Gredel (1999). Some of the absorption lines of the CN red system are unresolved blends of spin-rotation components. Relevant line blends studied here are $[R_2(1) + {}^RQ_{21}(1)]$, $[Q_2(1) + {}^QP_{21}(1)]$, and $[{}^QR_{12}(1) + Q_1(1)]$, with effective wavelengths near 9142.838 Å, 9147.203 Å, and 9190.113 Å, respectively, in the (1, 0) band, and 7873.987 Å, 7877.191 Å, and 7908.954 Å, respectively, in the (2, 0) band. The effective wavelengths are weighted averages obtained from the wavelengths given by van Dishoeck & Black (1989) for the various spin-rotation components, with the corresponding oscillator strengths used as weight.

The equivalent width of a spin-rotation line blend with contributions from the $(N'' = 1, J'' = \frac{1}{2})$ and $(N'' = 1, J'' = \frac{3}{2})$ levels is given by $W_\lambda = \frac{\pi e^2}{mc^2}\lambda^2\{N(1,\frac{1}{2})/f_{J',J''=\frac{1}{2}} + N(1,\frac{3}{2})/f_{J',J''=\frac{3}{2}}\}$. We assume that the spin-rotational levels (N'', J'') with the same rotational quantum number N'' are populated according to their statistical weights. Total column densities $N(1) = N(1,\frac{1}{2}) + N(1,\frac{3}{2})$ are then given by $N(1) = 3 \times N(1,\frac{1}{2})$ or $N(1) = 1.5 \times N(1,\frac{3}{2})$. We obtain $W_\lambda = \frac{\pi e^2}{mc^2}\lambda^2 N(1) f(v'v'') f_{\rm eff}$, with an effective rotational oscillator strength of $f_{\rm eff} = (f_{J'J''=\frac{1}{2}}/3.0 + f_{J'J''=\frac{3}{2}}/1.5)$. As above, we factorise $f_{\rm eff} = p_{\rm eff} f(v'v'')$, $p_{\rm eff} = p_{J'J''=\frac{1}{2}}/3.0 + p_{J'J''=\frac{3}{2}}/1.5$, and derive values of $p_{\rm eff} = 0.228$, 0.167, and 0.305, respectively, for the $[R_2(1) + {}^RQ_{21}(1)]$, $[Q_2(1) + {}^QP_{21}(1)]$, and $[{}^QR_{12}(1) + Q_1(1)]$ blends. Absorption lines from $N'' = 0$ arise from one spin-rotation component only $(J'' = \frac{1}{2})$. For the $R_1(0)$, ${}^RQ_{21}(0)$, and ${}^SR_{21}(0)$ lines, $p_{\rm eff} = p_{J'J''=\frac{1}{2}} = 0.528$, 0.334, and 0.138, respectively. Column densities are inferred through the use of the

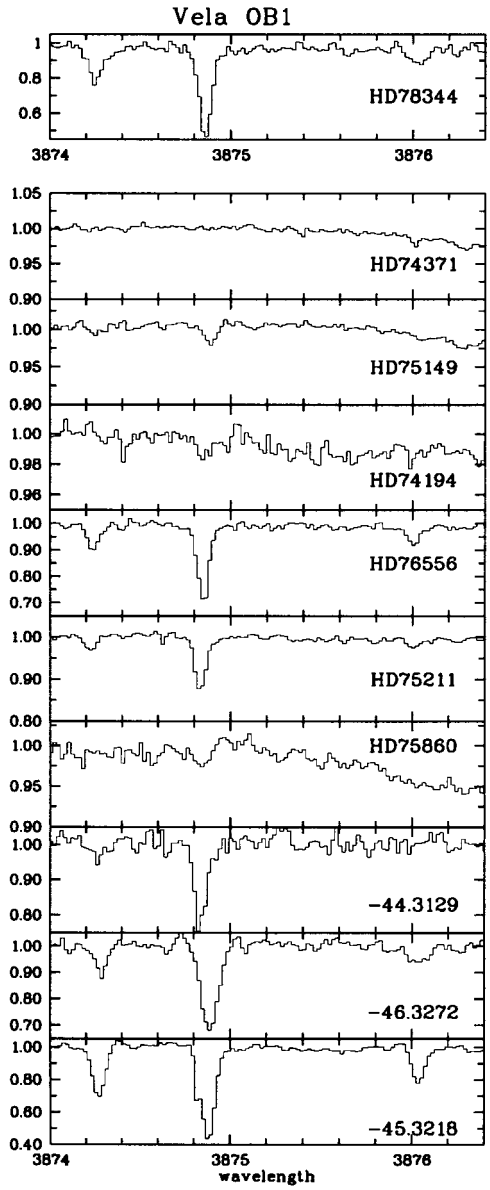

Fig. 2. Same as Fig. 1 for stars in Vela OB1.

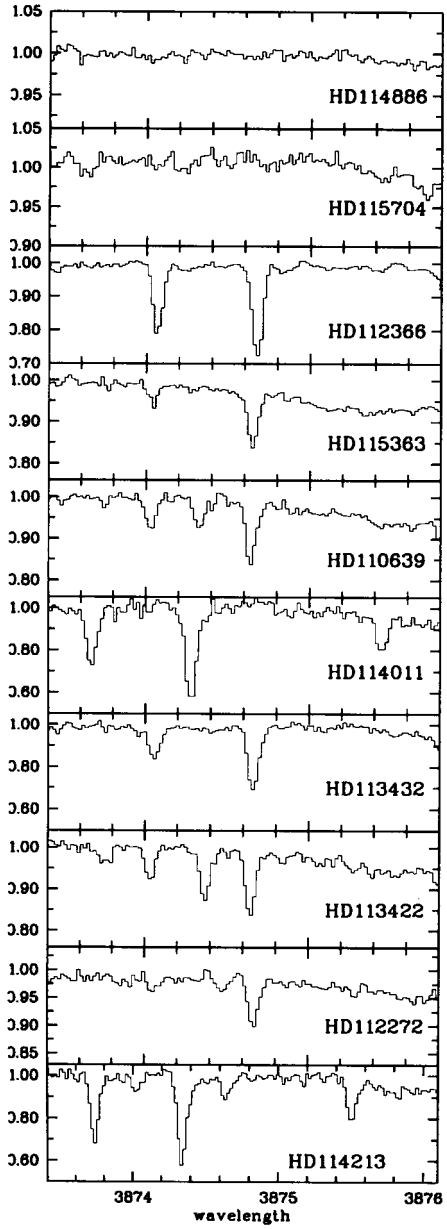

Fig. 3. Same as Fig. 1 for stars in Cen OB1.

Table 1. Data on the CN violet system toward NGC 2439 and Vela OB1[a].

star HD/CPD	line	$\lambda_{\rm hel}$	$V_{\rm hel}$	W_λ	$N_\infty(N'')$	$\overline{V_{\rm hel}}$
NGC2439						
63423	$R(1)$	3874.526	41.1	15.0(0.5)	4.9(0.2)	
	$R(0)$	3875.134	41.1	22.0(0.5)	4.8(0.1)	
	$P(1)$	3876.289	40.9	8.0(0.5)	5.3(0.3)	41.1
62150	$R(0)$	3875.092	37.8	1.5(0.5)	0.3(0.1)	37.8
61827	$R(1)$	3874.459	35.9	2.5(1.0)	0.8(0.3)	
	$R(0)$	3875.059	35.3	10.0(1.0)	2.2(0.2)	
	$P(1)$	3876.212	35.0	1.5(1.0)	1.0(0.7)	35.4
	$R(1)$	3874.526	41.1	2.0(1.0)	0.7(0.3)	
	$R(0)$	3875.145	41.9	10.0(1.0)	2.2(0.2)	
	$P(1)$	3876.285	40.6	2.0(1.0)	1.3(0.7)	41.4
62844	$R(1)$	3874.482	37.7	3.0(1.0)	1.0(0.3)	
	$R(0)$	3875.100	38.4	8.0(1.0)	1.8(0.2)	38.1
$-32°1734$	$R(1)$	3874.486	38.0	6.0(1.5)	2.0(0.5)	
	$R(0)$	3875.108	39.1	20.5(1.5)	4.5(0.3)	
	$P(1)$	3876.267	39.2	6.0(3.0)	4.0(2.0)	38.7
$-33°1768$	$R(1)$	3874.518	40.5	7.5(3.0)	2.5(1.0)	
	$R(0)$	3875.129	40.7	30.0(3.0)	6.6(0.7)	
	$P(1)$	3876.286	40.7	5.0(3.0)	3.3(2.0)	40.6
Vela OB1						
78344	$R(1)$	3874.256	20.2	20.0(3.0)	6.6(1.0)	
	$R(0)$	3874.861	20.0	46.0(3.0)	10.1(0.7)	
	$P(1)$	3876.030	20.9	11.0(3.0)	7.3(2.0)	20.2
75149	$R(0)$	3874.892	22.4	2.0(0.5)	0.4(0.1)	22.4
76556	$R(1)$	3874.240	19.0	7.5(1.0)	2.5(0.3)	
	$R(0)$	3874.849	19.0	23.0(1.0)	5.1(0.2)	
	$P(1)$	3876.005	19.0	6.0(1.0)	4.0(0.7)	19.0
75211	$R(1)$	3874.225	17.9	2.0(1.0)	0.7(0.3)	
	$R(0)$	3874.834	17.9	12.0(1.0)	2.6(0.2)	
	$P(1)$	3876.010	19.4	≤ 1.5	≤ 1.0	18.1
$-44°3129$	$R(0)$	3874.836	18.0	18.0(1.0)	4.0(0.2)	18.0
$-46°3272$	$R(1)$	3874.283	22.3	10.5(2.0)	3.5(0.7)	
	$R(0)$	3874.888	22.1	39.0(2.0)	8.6(0.4)	
	$P(1)$	3876.032	21.1	7.0(2.0)	4.6(1.3)	22.0
$-45°3218$	$R(1)$	3874.273	21.6	25.0(3.0)	8.3(1.0)	
	$R(0)$	3874.884	21.8	49.0(3.0)	10.8(0.7)	
	$P(1)$	3876.039	21.6	15.5(3.0)	10.2(2.0)	21.7

[a] $\lambda_{\rm hel}$ in Å, $V_{\rm hel}$ in km s^{-1}, W_λ in mÅ, N in 10^{12} cm^{-2}.

experimental band oscillator strengths of $f_{10} = 1.5 \times 10^{-3}$ and $f_{20} = 7.6 \times 10^{-4}$ of Davis et al. (1986).

The spectra covering the (2, 0) and (1, 0) bands of the CN red system are displayed in Figs. 4 and 5, respectively. The spectra are dominated by strong telluric absorption features. Filled symbols identify detected CN lines, and open symbols mark features used to infer upper limits in the CN column densities. Toward CPD−33°1768, HD 113432, HD 114011, and HD 114213, CN absorption lines are detected in both bands of the red system. A few of the other stars show marginal detections with equivalent widths of 2–3 standard deviations, mainly in the $R_1(0)$ line of both bands. Table 3 summarises the measurements in the CN red system, with the star, the band and the line designation, the corresponding spin and rotational quantum numbers J'' and N'', the heliocentric wavelength in Å, the corresponding heliocentric velocity in km s^{-1}, the measured equivalent width W_λ in mÅ, and the inferred column density $N(N'', J'')$, in Cols. 1–8, respectively. Note that our analysis yields total column densities $N(1)$ for line blends, but column densities in individual spin-rotation levels for single lines such as the $R_1(1)$ line. Total column densities in the $N'' = 0$ and $N'' = 1$ rotational levels are given in Cols. 9 and 10, respectively, and are averages of values obtained in the (1, 0) and (2, 0) bands when available, weighted with the oscillator strengths. The corresponding rotational excitation temperatures $T_{\rm red}$ are given in Col. 11 of Table 3.

Table 2. Data on the CN violet system toward Cen OB1[a].

star HD	line	$\lambda_{\rm hel}$	$V_{\rm hel}$	W_λ	$N_\infty(N'')$	$\overline{V_{\rm hel}}$
112366	$R(1)$	3874.064	5.4	15.5(2.0)	5.1(0.7)	
	$R(0)$	3874.671	5.3	20.0(2.0)	4.4(0.4)	
	$P(1)$	3875.833	5.7	11.0(2.0)	7.3(1.3)	5.4
115363	$R(1)$	3874.044	3.9	2.0(0.5)	0.7(0.2)	
	$R(0)$	3874.650	3.7	9.5(0.5)	2.1(0.1)	3.8
110639	$R(1)$	3874.031	2.9	6.0(0.5)	2.0(0.2)	
	$R(0)$	3874.640	2.9	11.0(0.5)	2.4(0.1)	
	$P(1)$	3875.796	2.9	2.5(0.5)	1.7(0.3)	2.9
	$R(1)$	3873.746	−19.2	1.5(0.5)	0.5(0.2)	
	$R(0)$	3874.324	−21.5	4.5(0.5)	1.0(0.1)	−20.6
114011	$R(1)$	3873.669	−25.1	22.0(1.0)	7.3(0.3)	
	$R(0)$	3874.280	−24.9	41.5(1.0)	9.1(0.2)	
	$P(1)$	3875.444	−24.3	13.5(1.0)	8.9(0.7)	−24.9
113432	$R(1)$	3874.057	4.9	12.0(1.0)	4.0(0.3)	
	$R(0)$	3874.662	4.6	24.5(1.0)	5.4(0.2)	
	$P(1)$	3875.819	4.6	5.5(1.0)	3.6(0.7)	4.7
113422	$R(1)$	3873.751	−18.8	3.5(1.0)	1.2(0.3)	
	$R(0)$	3874.368	−18.1	7.5(1.0)	1.7(0.2)	−18.5
	$R(1)$	3874.033	3.0	5.0(1.0)	1.7(0.3)	
	$R(0)$	3874.647	3.4	10.5(1.0)	2.3(0.2)	
	$P(1)$	3875.793	2.6	2.0(1.0)	1.3(0.7)	3.2
112272	$R(1)$	3874.054	4.6	1.5(0.5)	0.5(0.2)	
	$R(0)$	3874.673	5.5	5.5(0.5)	1.2(0.1)	5.0
114213	$R(1)$	3873.734	−20.1	22.0(1.0)	7.3(0.3)	
	$R(0)$	3874.343	−20.0	32.0(1.0)	7.0(0.2)	
	$P(1)$	3875.506	−19.5	14.5(1.0)	9.6(0.7)	−20.0
	$R(1)$	3874.024	2.3	1.5(1.0)	0.5(0.3)	
	$R(0)$	3874.642	3.1	8.0(1.0)	1.8(0.2)	
	$P(1)$	3875.827	5.3	2.0(1.0)	1.3(0.7)	3.2

[a] $\lambda_{\rm hel}$ in Å, $V_{\rm hel}$ in km s^{-1}, W_λ in mÅ, N in 10^{12} cm^{-2}.

2.3. The (0, 0) band of the CH $B\,^2\Sigma^- – X\,^2\Pi$ system

The spectra taken with the CAT cover the $R_2(1)$ (3878.774 Å), $[Q_2(1) + {}^QR_{12}(1)]$ (3886.409 Å), and the ${}^PQ_{12}(1)$ (3890.217 Å) lines of the (0, 0) band of the B $^2\Sigma^-$–X $^2\Pi$ system of CH. These additional data are most useful as supplements to previously reported CH column densities and radial velocities (Gredel 1997). We use the molecular parameters employed by Gredel et al. (1993) to convert measured equivalent widths and wavelengths into column densities and radial velocities. The measurements are summarised in Tables 4 and 5, with the star, the heliocentric wavelength in Å, the heliocentric velocity in km s^{-1}, the measured equivalent width W_λ in mÅ, and the corresponding column density N in units of 10^{13} cm^{-2}, listed in Cols. 1–5, respectively. Columns 6 and 7 contain the average heliocentric CH velocity and the average column density $\overline{N}$, obtained from the individual measurements weighted by the rotational oscillator strengths.

3. Analysis

3.1. The CN Doppler parameter b(CN) and final CN column densities

Total CN column densities N_∞ obtained from the violet system data in the limit of unsaturated lines are given by $N_\infty = \Sigma N_\infty(N'')$, where the summation is carried out over rotational levels $N'' = 0, 1$ and 2. $N_\infty(0)$ and $N_\infty(1)$ are taken from Col. 6 of Tables 1 and 2, and $N_\infty(2)$ is calculated from $N_\infty(2) = 5 \times N_\infty(0) \times {\rm e}^{-16.325/T_\infty}$. T_∞ is the CN rotational excitation temperature which is obtained from the population density in $N'' = 0$ and 1, viz. $T_\infty = 5.4419$ K ln $(3 \times N_\infty(0)/N_\infty(1))$. The values of N_∞ and T_∞ are given in Cols. 2 and 3 of Table 6, respectively. Uncertainties in N_∞ and T_∞ resulting from measurement uncertainties in the equivalent widths are given in parentheses. Column densities marked with an asterisk are those where $N_\infty(1)$ is not available from the observations, and where N_∞ was calculated by assuming a rotational excitation temperature of $T_\infty = 2.7$ K.

The absorption lines of the CN (0, 0) violet system are saturated in general (cf. Gredel et al. 1991), which implies that the values N_∞ are only lower limits to the total CN column densities. A curve of growth (COG) analysis is needed to obtain saturation corrections. The method requires knowledge of the micro- and macro-turbulent velocity dispersions, which may be described in terms of Doppler parameters b and the general velocity structure of the line of sight. If the spectral lines are resolved, a generally robust method to infer column densities is to characterise the macroscopic velocity structure in terms of absorption components, and to calculate for each component the column density which corresponds to its microscopic velocity dispersion given by its Doppler b-value. For resolved lines, b may be determined from the full width at half maximum of the absorption component. The Doppler parameters b may be different for the various components. Jenkins (1986) demonstrated that this approach does produce sensible results for total column densities. A detailed discussion of the analysis of moderately saturated lines and the effects of the velocity structure is also given by Black & van Dishoeck (1988).

Our spectral resolution is too coarse to resolve the CN line profile, and indirect methods are applied to infer Doppler parameters b(CN). In cases where unresolved velocity structure is present, the indirect methods provide an effective Doppler parameter which is generally larger than the Doppler parameters of the individual components. While the total CN column densities inferred from e.g. the comparison of unsaturated and saturated absorption lines which arise from a common rotational level are rather robust, the derived effective Doppler paramters may not properly describe the microscopic velocity dispersion. This point is further discussed in Sect. 3.1.4.

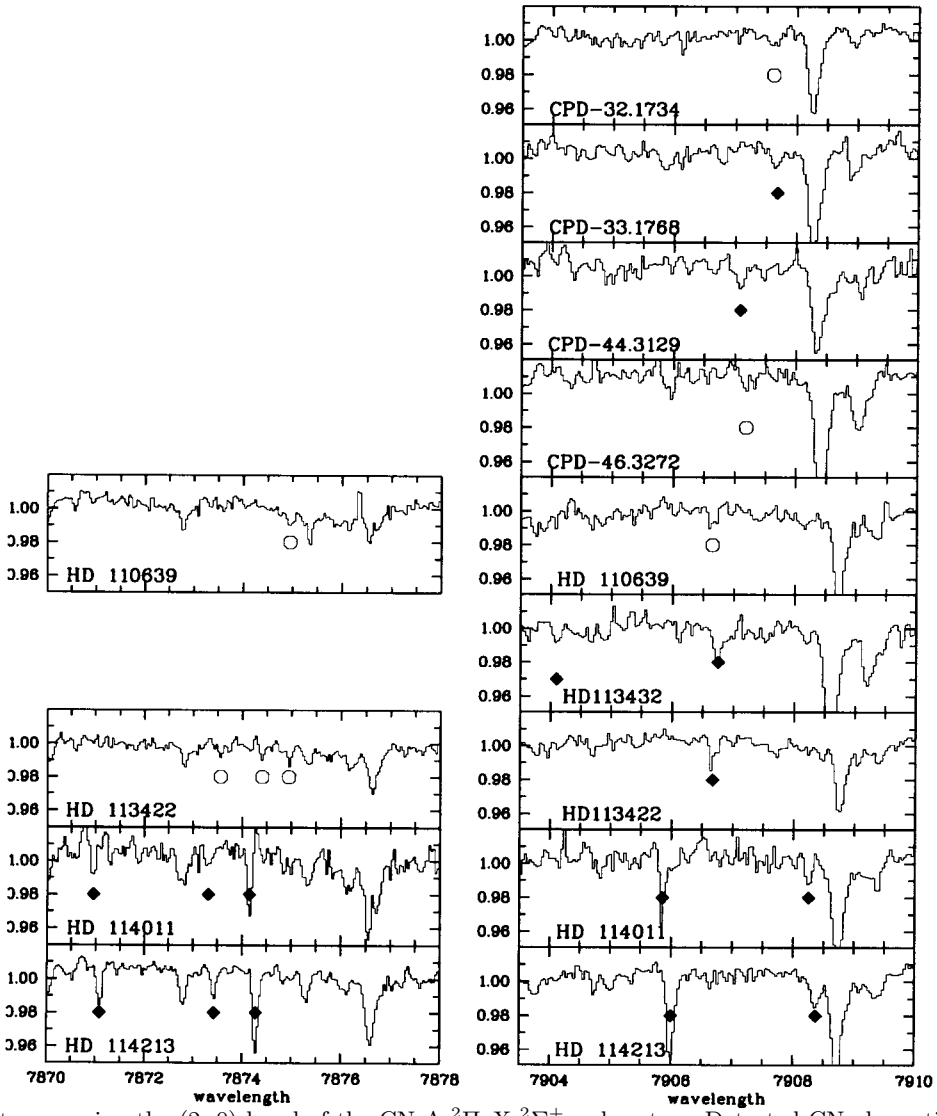

Fig. 4. Stellar spectra covering the (2, 0) band of the CN A $^2\Pi$–X $^2\Sigma^+$ red system. Detected CN absorption lines are marked by the filled symbol. Open symbols indicate marginal detections or spectral features which are used to infer upper limits on the CN column density.

3.1.1. The doublet ratio method

The doublet ratio method (Strömgren 1948; Münch 1968) compares the strengths of two absorption lines arising from the same rotational level but having different oscillator strengths. If saturation effects prevail, the column density inferred from each line is different. A COG analysis with an iteration on b is performed until the column densities agree. Here we compare the strength of the $R(1)$ and $P(1)$ absorption lines in the (0, 0) band of the CN violet system, both of which arise from the $N'' = 1$ rotational level. The doublet ratio DR is given by $DR = W_\lambda(R(1))/W_\lambda(P(1))$. In the limit of unsaturated lines and the absence of measurement errors, the doublet ratio is determined by the ratio of the product of oscillator strengths and rest wavelengths of the two absorption lines, which in the present case is $DR = 1.9973$. If both lines are heavily saturated, the doublet ratio approaches the value of ≈1. The difference in the oscillator strengths and wavelengths between the two lines is rather small, however, and very accurate equivalent widths are required for a reliable determination of b.

We follow Gredel et al. (1991) and treat the individual spin rotation components explicitly in the COG analysis. A large table of W_λ and b is computed for the $R(0)$, $R(1)$, and $P(1)$ lines of the (0, 0) band of the CN violet system. Column densities are obtained by cubic spline interpolation within this table. The results of the analysis are given in Table 6, with the CN Doppler parameter b_{DR} which is inferred from the doublet ratio listed in Col. 4. The corresponding total CN column density N_{DR} is given in Col. 5, and the CN excitation temperature T_{DR} obtained from $N_{DR}(0)$ and $N_{DR}(1)$ is presented in Col. 6.

Accurate determinations of $b_{\rm DR}$ are obtained for HD 114011 and HD 114213(−20), with values of 0.98 and 0.75 $\mathrm{km\,s^{-1}}$, respectively. The value in parenthesis added to the star-number indicates the radial velocity of the CN absorption component in cases where more than 1 component appears. The uncertainties in measured equivalent

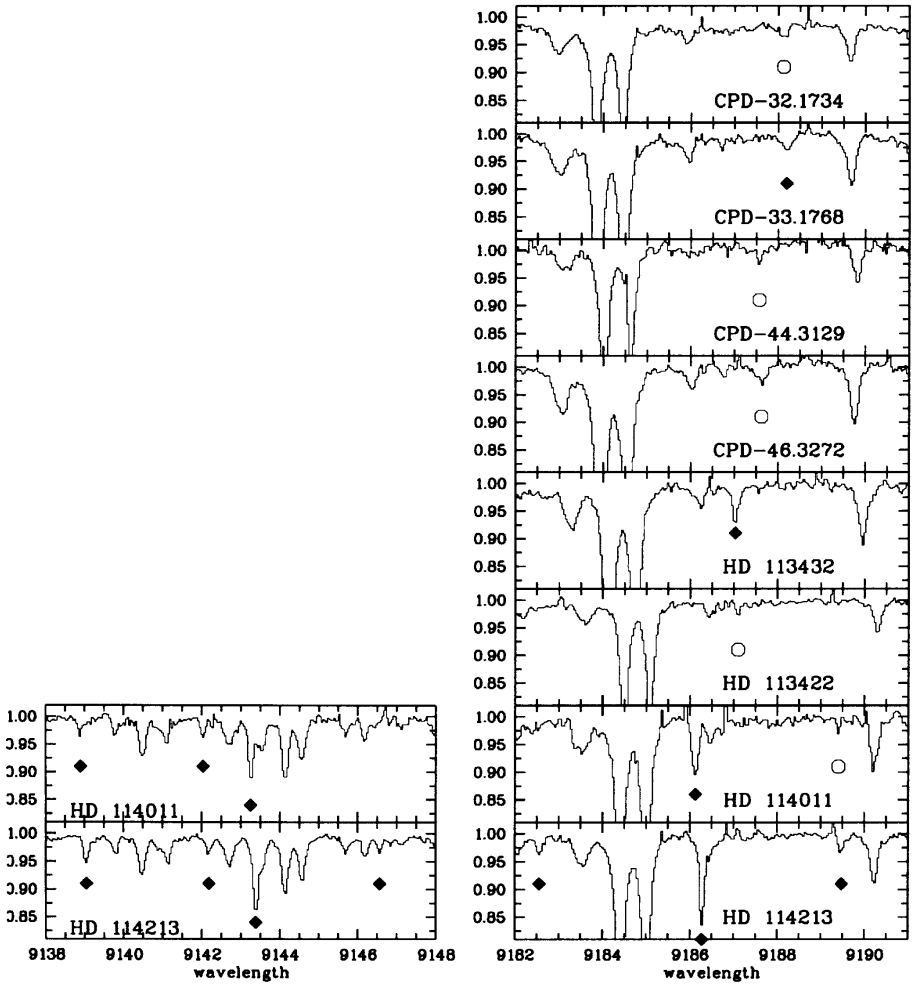

Fig. 5. Same as Fig. 4 for stellar spectra covering the (1, 0) band of the CN red system.

widths allow for ranges in b of 0.6–2.3 $\mathrm{km\,s^{-1}}$ toward HD 114011 and 0.5–1.25 $\mathrm{km\,s^{-1}}$ toward HD 114213(−20). Resulting ranges in total CN column densities are given in Col. 5 of Table 6.

The doublet ratios for gas toward HD 63423, HD 78344, and CPD−45°3218 imply values for b_{DR} of 1.95, 1.75, and 1.1 $\mathrm{km\,s^{-1}}$, respectively. The uncertainties in the measured equivalent widths allow for ranges of $0 < b < \infty$ toward HD 78344 and CPD−45°3218, which is too large to infer uncertainties in N_{DR}. Toward HD 63423, a lower limit of $b \geq 0.8$ $\mathrm{km\,s^{-1}}$ is obtained. The doublet ratio gives N_{DR} of 12.5×10^{12} $\mathrm{cm^{-2}}$ and a range which arises from the uncertainty in b of $(10-17) \times 10^{12}$ $\mathrm{cm^{-2}}$. These values are adopted as final CN column density in the discussion of Sect. 4.2. Toward HD 78344, we adopt a total CN column density of 26.7×10^{12} $\mathrm{cm^{-2}}$ and a range of $(22-32) \times 10^{12}$ $\mathrm{cm^{-2}}$. Final CN column densities used in Sect. 4.2 are given in bold face in Table 6.

In a few cases, doublet ratios larger than 2 or smaller than 1 are obtained, which is unphysical. Doublet ratios larger than two toward HD 110639(+3), HD 113432, and HD 113422(+3) are caused by measurement errors. A ratio close to 2 suggests that the CN lines are not, or only weakly, saturated. The CN absorption lines toward HD 110639(+3) and HD 113422(+3) are relatively weak indeed, and saturation effects are not significant even for small b-values. A doublet ratio smaller than 1 is obtained toward HD 114213(+3), and small values (<1.5) are obtained toward CPD−32°1734, CPD−33°1768, CPD−46°3272, and HD 112366. Toward HD 114213(+3), the absorption lines are very weak, and the measurement uncertainties allow for doublet ratios of $1 < DR < 2$. Toward the other stars, the small doublet ratios derived from the measurements would indicate that the absorption lines are heavily saturated. For CPD−32°1734, CPD−33°1768, HD 76556, CPD−46°3272, and HD 112366, Doppler parameters of $b_{DR} < 0.2$ $\mathrm{km\,s^{-1}}$ are derived, which are very low. Such low values of b would imply extremely large CN column densities, with $N_{DR} > 10^{15}$ $\mathrm{cm^{-2}}$ in general. Moreover, the resulting CN excitation temperatures were less than 2 K, which is unphysical. The measurement uncertainties in W_λ allow for a range of $0 < b < \infty$ $\mathrm{km\,s^{-1}}$ toward the latter five stars, too large to infer meaningful values for N_{DR}.

The doublet ratio is not applied to the two velocity components toward HD 61827, because the corresponding equivalent widths are obtained from a 2-component Gaussian fit to a partly resolved line profile. The uncertainties in the equivalent widths toward the remaining

Table 3. Absorption lines in the (1, 0) and (2, 0) band of the CN A $^2\Pi$–X $^2\Sigma^+$ red system.

star	band, line	J''	N''	$\lambda_{\rm hel}$	$V_{\rm hel}$	W_λ	$N(J'', N'')$	$N(0)$	$N(1)$	$T_{\rm red}$
				Å	km s^{-1}	mÅ	10^{12} cm^{-2}			K
CPD−32°1734	$(2,0)R_1(0)$	$\frac{1}{2}$	0	7907.615	38.4	≤1.0	≤4.5	≤5.4	...	...
	$(1,0)R_1(0)$	$\frac{1}{2}$	0	9188.122	38.7	≤3.5	≤5.9			
CPD−33°1768	$(2,0)R_1(0)$	$\frac{1}{2}$	0	7907.680	40.8	1.5(0.5)	6.8(2.0)	9.6(2.0)	...	...
	$(1,0)R_1(0)$	$\frac{1}{2}$	0	9188.194	41.0	6.5(1.0)	11.0(2.0)			
CPD−44°3129	$(2,0)R_1(0)$	$\frac{1}{2}$	0	7907.086	18.4	≤1.5	≤6.8	≤6.5	...	...
	$(1,0)R_1(0)$	$\frac{1}{2}$	0	9187.570	20.7	≤3.5	≤5.9			
CPD−46°3272	$(2,0)R_1(0)$	$\frac{1}{2}$	0	7907.185	22.1	≤2.0	≤9.0	≤10.8	...	...
	$(1,0)R_1(0)$	$\frac{1}{2}$	0	9187.617	22.2	≤7.0	≤11.8			
HD 110639	$(2,0)^RQ_{21}(0)$	$\frac{1}{2}$	0	7874.952	4.0	≤1.0	≤7.1	≤6.8	...	...
	$(2,0)R_1(0)$	$\frac{1}{2}$	0	7906.646	1.7	≤1.5	≤6.8			
HD 113432	$(2,0)R_1(0)$	$\frac{1}{2}$	0	7906.748	5.6	1.5(1.0)	6.8(5.0)	13.5(3.0)	≤10.5	...
	$(1,0)R_1(0)$	$\frac{1}{2}$	0	9187.030	3.1	10.0(1.0)	16.9(2.0)			
	$(2,0)R_1(1)$	$\frac{3}{2}$	1	7904.097	7.6	≤1.0	≤7.1			
HD 113422	$(2,0)^RQ_{21}(0)$	$\frac{1}{2}$	0	7874.405	−16.8	≤1.0	≤7.2	≤7.2	≤10.5	
	$(2,0)[R_2(1)+^RQ_{21}(1)]$	$\frac{1}{2}+\frac{3}{2}$	1	7873.562	−16.2	≤1.0	≤10.5			
	$(2,0)^RQ_{21}(0)$	$\frac{1}{2}$	0	7874.945	3.7	≤1.0	≤7.2	≤5.3	...	...
	$(2,0)R_1(0)$	$\frac{1}{2}$	0	7906.667	2.5	≤2.0	≤9			
	$(1,0)R_1(0)$	$\frac{1}{2}$	0	9187.098	5.3	≤2.5	≤4.2			
HD 114011	$(2,0)^SR_{21}(0)$	$\frac{1}{2}$	0	7870.958	−26.0	2.0(1.0)	34.8(17.0)	27.5(5.0)	13.1(6.5)	3.0
	$(2,0)^RQ_{21}(0)$	$\frac{1}{2}$	0	7874.151	−26.5	4.0(1.0)	28.7(7.0)			
	$(2,0)R_1(0)$	$\frac{1}{2}$	0	7905.856	−28.2	3.5(1.0)	15.8(5.0)			
	$(1,0)^SR_{21}(0)$	$\frac{1}{2}$	0	9138.896	−25.6	4.5(3.0)	29.4(19.0)			
	$(1,0)^RQ_{21}(0)$	$\frac{1}{2}$	0	9143.247	−26.1	12.0(3.0)	32.4(8.0)			
	$(1,0)R_1(0)$	$\frac{1}{2}$	0	9186.126	−26.4	17.0(5.0)	28.7(8.0)			
	$(2,0)[R_2(1)+^RQ_{21}(1)]$	$\frac{1}{2}+\frac{3}{2}$	1	7873.318	−25.4	≤1.0	≤10.5			
	$(2,0)[^QR_{12}(1)+Q_1(1)]$	$\frac{1}{2}+\frac{3}{2}$	1	7908.253	−26.5	2.0(1.0)	12.3(6.0)			
	$(1,0)[R_2(1)+^RQ_{21}(1)]$	$\frac{1}{2}+\frac{3}{2}$	1	9142.036	−26.3	5.0(3.0)	19.8(12.0)			
	$(1,0)[^QR_{12}(1)+Q_1(1)]$	$\frac{1}{2}+\frac{3}{2}$	1	9189.405	−23.1	≤2.5	≤7.0			
HD 114213	$(2,0)^SR_{21}(0)$	$\frac{1}{2}$	0	7871.081	−21.4	3.0(1.0)	52.2(17.0)	31.9(5.0)	21.1(5.0)	3.6
	$(2,0)^RQ_{21}(0)$	$\frac{1}{2}$	0	7874.277	−21.7	6.0(1.0)	43.1(7.0)			
	$(2,0)R_1(0)$	$\frac{1}{2}$	0	7905.996	−22.9	7.0(1.0)	31.5(5.0)			
	$(1,0)^SR_{21}(0)$	$\frac{1}{2}$	0	9139.047	−20.6	7.0(3.0)	45.7(20.0)			
	$(1,0)^RQ_{21}(0)$	$\frac{1}{2}$	0	9143.377	−21.8	10.0(3.0)	27.0(8.0)			
	$(1,0)R_1(0)$	$\frac{1}{2}$	0	9186.277	−21.4	15.0(3.0)	25.4(5.0)			
	$(2,0)[R_2(1)+^RQ_{21}(1)]$	$\frac{1}{2}+\frac{3}{2}$	1	7873.426	−21.3	2.0(1.0)	20.9(10.0)			
	$(2,0)[^QR_{12}(1)+Q_1(1)]$	$\frac{1}{2}+\frac{3}{2}$	1	7908.372	−22.0	4.0(2.0)	24.6(12.0)			
	$(1,0)[R_2(1)+^RQ_{21}(1)]$	$\frac{1}{2}+\frac{3}{2}$	1	9142.186	−21.3	5.0(3.0)	19.8(12.0)			
	$(1,0)[Q_2(1)+^QP_{21}(1)]$	$\frac{1}{2}+\frac{3}{2}$	1	9146.557	−21.1	5.0(3.0)	27.0(16.0)			
	$(1,0)R_1(1)$	$\frac{3}{2}$	1	9182.557	−21.5	5.0(2.0)	13.4(5.0)			
	$(1,0)[^QR_{12}(1)+Q_1(1)]$	$\frac{1}{2}+\frac{3}{2}$	1	9189.476	−20.7	5.0(3.0)	14.0(8.0)			

stars are too large to obtain a reliable determination of $b_{\rm DR}$.

Toward HD 63423, HD 78344, CPD−45°3218, HD 110639(+3), HD 114011, HD 113432, HD 113422(+3), and HD 114213(−20), rotational excitation temperatures T_{DR} which result from the column densities obtained with b_{DR} are given in Col. 6 of Table 6. For CPD−45°3218, T_{DR} is 2.0 K which is too low. The CN data toward this star is analysed further in Sect. 3.1.4. A low value of 2.3 K is also obtained toward HD 114011, but the range in T_{DR} allowed by the range in b_{DR} is 1.2–3.5 K. Toward the other stars, the values are T_{DR} = 2.8–5 K. The relatively high values toward HD 63423 and HD 110639(+3) may indicate the presence of unresolved velocity components because saturation affects the ground state lines to a greater extent. This is because the population density in $N''=0$ is always larger than in $N''=1$ and because the $R(0)$ line of the $(0,0)$ band of the violet system has a larger oscillator strength than the $R(1)$ or $P(1)$ lines. The high values may also arise from measurement errors in the rotational lines of the $(0,0)$ band of the violet system.

3.1.2. Comparison of data on the CN violet and red systems

In a method similar to the doublet ratio method, saturation effects are determined from a comparison of column

Table 4. Data for the CH B $^2\Sigma^-$–X $^2\Pi$ system toward CMa OB1 and NGC 2439.

star HD/CPD	$\lambda_{\rm hel}$ Å	$V_{\rm hel}$ km s^{-1}	W_λ mÅ	N 10^{13} cm^{-2}	$\overline{V_{\rm hel}}$ km s^{-1}	$\overline{N}$ 10^{13} cm^{-2}
54662	3886.870	35.5	1.5(0.5)	0.7(0.2)	35.5	0.7(0.2)
63423	3879.301	40.7	2.5(0.5)	3.5(0.7)		
	3886.927	39.9	9.0(0.5)	4.2(0.2)		
	3890.747	40.8	3.5(0.5)	2.4(0.3)	40.3	3.5(0.1)
62150	3879.241	36.0	2.0(1.0)	2.8(1.4)		
	3886.902	38.0	5.0(0.5)	2.3(0.2)		
	3890.726	39.2	3.0(1.0)	2.1(0.7)	38.0	2.3(0.1)
61827	3879.255	37.1	2.0(0.5)	2.8(0.7)		
	3886.879	36.2	5.0(0.5)	2.3(0.2)		
	3890.686	36.1	4.0(0.5)	2.8(0.3)	36.3	2.6(0.1)
	3886.956	42.1	3.0(0.5)	1.4(0.2)		
	3890.751	41.1	2.5(0.5)	1.7(0.3)	41.7	1.5(0.1)
62844	3879.270	38.3	3.5(0.5)	4.9(0.7)		
	3886.911	38.7	10.0(0.5)	4.7(0.2)		
	3890.725	39.1	6.0(0.5)	4.2(0.3)	38.7	4.6(0.1)
−32°1734	3886.908	38.4	12.0(2.0)	5.6(0.9)	38.4	5.6(0.9)
−33°1768	3886.902	38.0	19.0(5.0)	8.9(2.3)		
	3890.730	39.5	14.0(5.0)	9.8(3.5)	38.6	9.2(1.0)
78344	3890.477	20.0	8.5(2.0)	5.9(1.4)	20.0	5.9(1.4)
75149	3886.703	22.6	3.0(1.0)	1.4(0.5)	22.6	1.4(0.5)
74194	3886.693	21.9	2.5(0.5)	1.2(0.2)		
	3890.509	22.5	2.0(0.5)	1.4(0.3)	22.1	1.3(0.1)
76556	3886.668	19.9	7.5(1.0)	3.5(0.5)		
	3890.476	19.9	6.0(1.0)	4.2(0.7)	19.9	3.8(0.2)
75211	3886.736	25.2	1.5(0.5)	1.9(1.0)		
	3890.533	24.3	1.5(0.5)	2.4(1.0)	24.8	2.1(1.0)
75860	3879.065	22.5	2.0(1.0)	2.8(1.4)		
	3886.685	21.3	4.0(1.0)	1.9(0.5)	21.6	2.1(0.2)
−44°3129	3886.684	21.2	9.0(2.0)	4.2(0.9)		
	3890.493	21.2	10.0(3.0)	7.0(2.1)	21.2	5.3(0.5)
−46°3272	3886.685	21.3	12.0(1.0)	5.6(0.5)		
	3890.490	21.0	7.5(3.0)	5.2(2.1)	21.2	5.5(0.4)
−45°3218	3879.061	22.1	5.0(1.5)	7.0(2.1)		
	3886.688	21.5	11.0(1.5)	5.1(0.7)		
	3890.506	22.2	13.5(1.5)	9.4(1.0)	21.8	6.9(0.2)

densities derived from absorption lines which arise in different electronic bands. For CN, a comparison between the violet and red systems works particularly well, because the difference in oscillator strengths is very large. In the following, we treat the lines in the CN red system as unsaturated, and perform a COG analysis for data involving the violet system with an iteration on b until the column densities agree with those inferred from the red system. The Doppler parameters $b_{\rm VR}$ obtained in this way are listed in Col. 7 of Table 6; total CN column densities $N_{\rm VR}$ and rotational excitation temperatures $T_{\rm VR}$ are given in Cols. 8 and 9, respectively.

Very narrow ranges in $b_{\rm VR}$ are obtained toward the three stars in Cen OB1 which have accurate detections of absorption lines in the CN red system. We find $b_{\rm VR}$ = 0.6–0.8 km s^{-1} toward HD 113432, 1.05–1.25 km s^{-1} toward HD 114011, and 0.65–0.85 km s^{-1} toward HD 114213(−20). The Doppler parameters found for HD 114011 and HD 114213 agree remarkably well with those obtained from the doublet ratio method. Column densities $N(1)$ calculated for $b_{\rm VR}$ from the violet system data are 10.8×10^{12} cm^{-2} and 14.1×10^{12} cm^{-2} for HD 114011 and HD 114213(−20), respectively; these are adopted in the following as $N(1)$. These values are smaller than the column densities inferred from the red system data, $N(1) = (13.1 \pm 6.5) \times 10^{12}$ cm^{-2} and $N(1) = (21.1 \pm 5.0) \times 10^{12}$ cm^{-2} toward HD 114011 and HD 114213(−20), respectively, but the corresponding absorption lines in the red system are relatively weak and the measurement uncertainties are large. The total CN column densities derived toward HD 113432, HD 114011, and HD 114213(−20) from the comparison of violet and red system data are adopted as final in the discussion of Sect. 4.2.

Other sight lines yield useful information with this approach. For CPD−32°1734, CPD−44°3129, and

Table 5. CH B $^2\Sigma^-$–X $^2\Pi$ system data toward Cen OB1.

star HD/CPD	$\lambda_{\rm hel}$ Å	$V_{\rm hel}$ km s^{-1}	W_λ mÅ	N 10^{13} cm^{-2}	$\overline{V_{\rm hel}}$ km s^{-1}	$\overline{N}$ 10^{13} cm^{-2}
111904	3886.219	-14.6	1.0 (0.5)	0.5 (0.2)	−14.6	0.5 (0.2)
111973	3886.503	7.2	1.0 (0.5)	0.5 (0.2)	7.2	0.5 (0.2)
−59°4551	3886.252	-12.1	1.5 (0.5)	0.7 (0.2)	−12.1	0.7 (0.2)
	3886.465	4.3	1.5 (0.5)	0.7 (0.2)	4.3	0.7 (0.2)
114886	3886.465	4.3	1.0 (0.5)	0.5 (0.2)	4.3	0.5 (0.2)
112366	3878.841	5.2	3.0 (1.0)	4.2 (1.4)		
	3886.478	5.3	8.0 (1.0)	3.7 (0.5)		
	3890.292	5.8	5.0 (1.0)	3.5 (0.7)	5.4	3.7 (0.1)
115363	3886.454	3.5	5.0 (1.0)	2.3 (0.5)	3.5	2.3 (0.5)
110639	3878.512	−20.2	2.0 (1.0)	2.8 (1.4)		
	3886.137	−20.9	3.5 (1.0)	1.6 (0.5)		
	3889.943	−21.1	2.0 (0.5)	1.4 (0.3)	−20.9	1.8 (0.1)
	3878.810	2.8	1.5 (1.0)	2.1 (1.4)		
	3886.459	3.9	2.5 (1.0)	1.2 (0.5)		
	3890.247	2.3	1.5 (0.5)	1.0 (0.3)	3.2	1.3 (0.1)
114011	3878.430	−26.5	5.0 (3.0)	7.0 (4.2)		
	3886.084	−25.0	10.0 (3.0)	4.7 (1.4)		
	3889.886	−25.5	5.0 (3.0)	3.5 (2.1)	−25.4	4.7 (0.4)
113432	3886.180	−17.6	2.0 (1.0)	0.9 (0.5)	−17.6	0.9 (0.5)
	3878.847	5.6	3.0 (1.5)	4.2 (2.1)		
	3890.277	4.6	4.5 (1.0)	3.1 (0.7)		
	3886.469	4.6	8.0 (1.0)	3.7 (0.5)	4.8	3.5 (0.5)
113422	3886.173	−18.2	5.5 (1.5)	2.6 (0.7)		
	3889.980	−18.2	3.0 (1.0)	2.1 (0.7)	−18.2	2.4 (0.3)
	3886.455	3.5	2.5 (1.0)	1.2 (0.5)		
	3890.264	3.6	2.5 (1.0)	1.7 (0.7)	3.6	1.4 (0.2)
112272	3878.649	−9.6	2.5 (1.5)	3.5 (2.1)		
	3886.302	−8.2	6.0 (0.5)	2.8 (0.2)		
	3890.111	−8.2	4.0 (0.5)	2.8 (0.3)	−8.4	2.9 (0.1)
	3878.825	3.9	1.5 (1.5)	2.1 (2.1)		
	3886.462	4.1	5.5 (0.5)	2.6 (0.2)		
	3890.268	3.9	4.5 (0.5)	3.1 (0.3)	4.0	2.7 (0.1)
114213	3886.149	−20.0	7.0 (1.5)	3.3 (0.7)		
	3889.967	−19.2	8.5 (2.0)	5.9 (1.4)	−19.7	4.3 (0.4)
	3886.428	1.5	4.0 (1.0)	1.9 (0.5)		
	3890.256	3.0	4.5 (2.0)	3.1 (1.4)	2.1	2.4 (0.3)

CPD−46°3272, the upper limits in $N'' = 0$ obtained from the $R_1(0)$ lines in the (1,0) and (2,0) bands of the CN red system (cf. Table 3) indicate lower limits in b_{VR} of 2, 0.75, and 3 km s^{-1}, respectively. The values N_{VR} given in Col. 8 of Table 6 are column densities obtained for the lowest Doppler parameters b_{VR}. These values may be considered as upper limits on the total CN column density. Toward CPD−46°3272, we suggest a final CN column density of $(14 \pm 1) \times 10^{12}$ cm^{-2}. For CPD−33°1768, the column density $N(0)$ inferred from the violet system is brought into agreement with results on the red system for a Doppler parameter of $b_{VR} = 1.75$ km s^{-1}, but a range of 1.25 km s^{-1} $< b < \infty$ km s^{-1} is allowed by the uncertainties in the equivalent widths of the $R(0)$ line in the violet system.

Rotational excitation temperatures T_{VR} inferred from the population distributions in $N'' = 0$ and $N'' = 1$ are listed in Col. 9 of Table 6. Calculated temperatures are in the range of 2.5–3.2 K. Toward HD 114011, HD 113432, and HD 114213(+3), uncertainties in $T_{\rm VR}$ of 0.2–0.3 K are given in parentheses. Toward the other stars, uncertainties are significantly larger.

3.1.3. Comparison with data on CO emission lines

The width of millimetre CO emission lines may be used to estimate b(CN). Such observations resolve the CO line profiles in general, and the CO Doppler parameter $b_{\rm CO}$ is obtained from the full width at half maximum ΔV: $b_{\rm CO} = \Delta V/1.665$. We observed CO millimetre emission using the Swedish-ESO SEST telescope on La Silla, with a velocity resolution of 0.14 km s^{-1} at the frequency of the $J = 1 \rightarrow 0$ CO line. A complete description of the CO data will be given elsewhere. Here we proceed to

Table 6. Summary of CN analysis[a].

star HD/CPD	N_∞	T_∞	b_{DR}	N_{DR}	T_{DR}	b_{VR}	N_{VR}	T_{VR}	$b^\dagger_{\rm CO}$	$N_{b(\rm CO)}$	$T_{b(\rm CO)}$	$N_{b=1}$	$T_{b=1}$
63423	10.9(0.2)	5.2(0.3)	$1.95^{+\infty}_{-1.2}$	$\mathbf{12.5^{+4.5}_{-2.5}}$	4.8				c			14.7(1.0)	4.2(0.3)
62150	0.4(0.3)*	(2.7)							n			**0.5**(**0.3**)*	(2.7)
61827(+35)	3.1(0.4)	2.7(0.7)							c			**3.6**(**0.7**)	2.6(0.9)
61827(+41)	3.2(0.4)	2.7(0.7)							c			**3.6**(**0.7**)	2.6(0.9)
62844	2.8(0.4)	3.3(0.9)							n			**3.1**(**0.6**)	3.1(1.0)
−32°1734	7.3(0.6)	3.3(0.6)	<0.1	–		≥2.0	≤8.5	3.2	c			**10.0**(**2.0**)	2.9(0.8)
−33°1768	**9.5**(**1.2**)	2.8(0.7)	<0.1	–		$1.75^{+\infty}_{-0.5}$	12.4	2.5	c			$17.1^{+6.6}_{-4.5}$	2.1(0.6)
78344	17.5(1.2)	3.6(0.5)	1.75	**26.7**(**5.0**)	2.9				1.0	77.3	1.8	77.3^{+46}_{-23}	1.8(0.4)
75149	0.6(0.2)*	(2.7)							c			**0.7**(**0.2**)*	(2.7)
76556	8.3(0.4)	3.3(0.3)	<0.1	–					0.7	15.5	2.4	$\mathbf{11.8^{+1.1}_{-1.4}}$	2.8(0.4)
75211	**3.3**(**0.4**)	2.4(0.7)							c			4.0(0.5)	2.1(0.6)
−44°3129	5.6(0.6)*	(2.7)				≥0.75	≤9.1*	(2.7)	c			**7.8**(**1.0**)*	(2.7)
−46°3272	12.6(1.0)	2.9(0.4)	<0.1	–		≥3.0	≤14.8	2.7	c			35.2(8.0)	1.8(0.3)
−45°3218	20.8(1.2)	4.2(0.6)	1.1	80.1	2.0				c			115^{+65}_{-36}	1.8(0.4)
112366	12.1(1.0)	$6.7^{+2.6}_{-1.6}$	<0.2	–					0.7	**19.0**(**2.0**)	5.1	$16.3^{+0.7}_{-4.5}$	$5.8^{+3.5}_{-1.6}$
115363	**2.8**(**0.2**)	2.4(0.4)							1.6	3.0	2.4	3.1(0.4)	2.3(0.3)
110639(−20)	1.5(0.2)	3.0(1.0)				≤0.1			0.55	**1.6**(**0.5**)	2.8	1.6(0.4)	2.9(1.0)
110639(+3)	4.5(0.2)	4.5(0.5)	∞	4.2	4.0				0.55	**5.7**(**0.5**)	3.3	5.0(0.5)	3.6(0.5)
114011	18.0(0.4)	4.3(0.3)	$0.98^{+1.3}_{-0.4}$	53.9^{+800}_{-34}	2.3(1.2)	1.15(0.1)	**37.9**(**4.0**)	2.7(0.2)	1.4	29.8	3.1	51.4^{+3}_{-8}	2.3(0.2)
113432	9.6(0.4)	3.8(0.4)	∞	9.2	3.8	0.7(0.1)	**18.8**(**3.0**)	2.5(0.3)	0.5	43.1	1.8	13.8(1.0)	3.0(0.4)
113422(−18)	2.9(0.4)	$4.7^{+2.3}_{-1.2}$				≤0.1			1.9	3.0	3.6	**3.2**(**0.5**)	3.6(1.0)
113422(+3)	4.0(0.4)	3.6(1.0)	∞	3.8	3.6	≤0.1			0.85	4.5	3.2	**4.4**(**1.0**)	3.2(1.2)
112272	1.8(0.4)	2.6(0.6)							c			**1.8**(**0.4**)	2.6(0.6)
114213(−20)	17.0(0.4)	5.6(0.5)	$0.75^{+0.5}_{-0.3}$	46.8^{+450}_{-22}	2.8(1.4)	0.75(0.1)	**46.8**(**10.0**)	2.8(0.3)	1.15	26.3	4.2	$29.4^{+0.6}_{-3}$	3.8(0.4)
114213(+3)	2.6(0.4)	$2.8^{+1.2}_{-0.8}$	<0.1	–					0.7	3.0	2.6	**2.8**(**0.8**)	2.7(1.0)

[a] N in 10^{12} cm^{-2}, b in km s^{-1}, T in K.
Values in bold face are CN column densities adopted in the analysis of Sect. 4.2.
† c identifies complex CO line profiles. n identifies lines of sight where CO is not detected.
* Derived from $N(0)$ and $T_{\rm ex}$ = 2.7 K.

calculate CN column densities $N_{b(\mathrm{CO})}$ using b_{CO} as the Doppler parameter for CN. The main disadvantage of this method is that emission from material behind the star may not easily be discriminated from the foreground material which is seen in absorption. For complex CO line profiles and for CO emission which is spread over a large range of radial velocities this uncertainty becomes prominent. In cases where the CO emission is narrow and appears at the velocity of the CN absorption lines, it is likely but not certain that CO and CN occupy the same parcels of gas. The velocity dispersions may be different anyway. Bucher & Glinski (1999) showed that care should be exercised when analysing the line profiles of diatomic molecules. In particular, the line profiles of molecules such as CH^+ and CH reflect the non-Boltzmann translational energy distribution at which the molecules are formed. This is because the random velocities of these molecules which result from H and H_2 reactions are not thermalised by collisions, and line profiles substantially broader than what is expected from a Boltzmann distribution at the kinetic temperature may result. The case is particularly pronounced for CH^+, which is removed upon every collision with H_2, and for CH to a lesser extent. For CN and CO, the effect is probably less pronounced as neither molecule is formed via reactions involving H and H_2 at the low temperatures which prevail in quiescent translucent clouds.

In Col. 10 of Table 6 we list the CO Doppler parameter b_{CO} obtained from those CO emission lines where the CO emission occurs in single Gaussians near the velocity of CN absorption. CO line profiles which are broad and complex and where the radial velocity of the emission is spread over many $\mathrm{km\,s^{-1}}$ are labelled with *c*. For those lines of sight, a de-composition of the CO line profile into multiple Gaussians is arbitrary. Lines of sight where CO is not detected, with CO antenna temperatures of $T_{\mathrm{A}}^{*} < 0.1$ K, are labelled with *n*. The resulting CN column densities $N_{b(\mathrm{CO})}$ and CN rotational excitation temperatures $T_{b(\mathrm{CO})}$ are presented in Cols. 11 and 12, respectively. Toward CPD−33°1768, HD 78344, HD 76556, CPD−44°3129, CPD−45°3218, and HD 115363, the rotational excitation temperatures calculated for b_{CO} are very low, suggesting the presence of unresolved velocity structure or of measurement errors in the equivalent widths. For the other stars, the inferred CN column densities are consistent with those inferred from the other methods, except toward HD 113432 where $N_{b(\mathrm{CO})}$ is very large. These findings provide additional confidence that the CN saturation corrections are realistic. Toward stars HD 112366, HD 110639(+3), and HD 110639(−20), we adopt $N_{b(\mathrm{CO})}$ as final values.

3.1.4. Other methods and final CN column densities

For star CPD−45°3218, the doublet ratio yields a value for b_{DR} of $\approx$1 $\mathrm{km\,s^{-1}}$, but the corresponding CN excitation temperature is $T_{DR} = 2.0$ K which is too low. The measurement errors are relatively low. Instead, we iterate on *b* until we obtain a CN excitation temperature which is close to T_{CMB}. We obtain 2.7 K for a Doppler value of 1.4 $\mathrm{km\,s^{-1}}$, yielding a total CN column density of 42×10^{12} $\mathrm{cm^{-2}}$. For $b = 1.5$ $\mathrm{km\,s^{-1}}$, $N = 38 \times 10^{12}$ $\mathrm{cm^{-2}}$ and $T = 2.86$ K. We suggest a value of $N = (40 \pm 10) \times 10^{12}$ $\mathrm{cm^{-2}}$ as the total CN column density toward CPD−45°3218.

Toward CPD−33°1768, the rotational excitation temperature is 2.8 K and decreases significantly for any saturation correction applied. As noted above, the decrease in the excitation temperature with decreasing Doppler parameter arises from the fact that $N(0)$ is more susceptible to optical depth effects. Toward CPD−33°1768, we use N_∞ as the final CN column density in the discussion of Sect. 4.2.

Toward HD 75211 and HD 115363, the CN excitation temperatures obtained from $N_\infty(0)$ and $N_\infty(1)$ are 2.4 K. Such low, and unphysical, values may result from measurement errors in the equivalent widths of the $R(0)$, $R(1)$, and $P(1)$ lines. In both cases, the absorption lines are relatively weak, and saturation corrections are not large. We adopt N_∞ as final CN column densities. For a few other stars, measured equivalent widths are small as well, and saturation effects are not significant even for Doppler parameters of $b \approx 0.5$ $\mathrm{km\,s^{-1}}$. Such is the case for HD 62150 and HD 75149, where we adopt the column densities obtained for a Doppler parameter of 1 $\mathrm{km\,s^{-1}}$ as final.

If all other methods fail and if there is no information whatsoever concerning the CN *b*-value, we adopt an ad hoc value of $b = 1.0$ $\mathrm{km\,s^{-1}}$ to infer CN column densities. The relatively reliable determinations of b_{DR} and b_{VR} toward HD 114011 and HD 114213(−20) suggest values of the order of 1 $\mathrm{km\,s^{-1}}$. The ultra-high resolution observations of Lambert et al. (1990), Crawford (1995), and Crawford (1997) toward ζ Oph, HD 169454, and two stars in the Scorpius-Centaurus association indicate $b(\mathrm{CN}) = 0.3$–0.7 $\mathrm{km\,s^{-1}}$ for single and resolved velocity components. We also note that high-resolution observations of a sample of some 20 stars in the Cep OB2 and Cep OB3 associations indicate CN Doppler parameters of 1 $\mathrm{km\,s^{-1}}$ (Pan & Federman, unpublished). For completeness, we list total CN column densities $N_{b=1}$ for all stars and corresponding excitation temperatures $T_{b=1}$ obtained with $b = 1.0$ $\mathrm{km\,s^{-1}}$ in Cols. 13 and 14 of Table 6, respectively. Uncertainties in $N_{b=1}$ and $T_{b=1}$ allowed by the uncertainties in the measured equivalent widths are given in parentheses. Values for $N_{b=1}$ derived toward CPD−32°1734, HD 76556, CPD−44°3129, HD 113422(−18), and HD 113422(+3) are adopted as final in Sect. 4.2.

An effective Doppler parameter of $b = 1$ $\mathrm{km\,s^{-1}}$ may be used for moderately saturated lines which are composed of 2–3 absorption components separated by 1–2 $\mathrm{km\,s^{-1}}$, if the total column density is $N(N'' = 0) < 10^{13}$ $\mathrm{cm^{-2}}$ and if the $b = 0.5 - 0.7$ $\mathrm{km\,s^{-1}}$ for each of the absorption components. For instance, we obtain for HD 76556 a total column density in $N'' = 0$ of $N(N'' = 0) = 11.1 \times 10^{12}$ $\mathrm{cm^{-2}}$ from the measured equivalent width of 23 mÅ in the $R(0)$

line of the CN blue system, if we assume that the line is formed from three velocity components separated by 2 km s^{-1} from each other, each component characterised by $b = 0.7$ km s^{-1}. A single component with an effective Doppler parameter of $b = 1$ km s^{-1}yields $N(N'' = 0) = 8.3 \times 10^{12}$ cm^{-2}. The column obtained in the limit for unsaturated lines is $N_\infty(N'' = 0) = 5.1 \times 10^{12}$ cm^{-2}.

For HD 61827(+35), HD 61827(+41), HD 62844, HD 112272, and HD 114213(+3), the CN excitation temperature inferred in the limit of $b \rightarrow \infty$ is 2.7 K and slightly smaller for $b = 1$ km s^{-1}. In all cases, the absorption lines are relatively weak and saturation corrections for Doppler parameters $b > 0.5$ km s^{-1} are small. For these clouds, we adopt the CN column densities inferred from $b = 1$ km s^{-1} as final.

3.2. Comparison of data on the CH $A\,^2\Delta$–$X\,^2\Pi$ and $B\,^2\Sigma^-$–$X\,^2\Pi$ systems

The observations of CH absorption lines in the (0, 0) band of the CH B–X system presented above provide an independent and useful check on the final CH column densities of Gredel (1997). Absorption from the (0, 0) band of the CH A $^2\Delta$–X $^2\Pi$ system toward the stars observed here was corrected for saturation effects using a CH Doppler parameter b(CH) of 1.5 km s^{-1} in general. The particular value is suggested by high-resolution observations of interstellar CH where the line profile has been resolved (e.g., Crane et al. 1995, Crawford 1995). In a few cases, the saturation corrections of Gredel (1997) are substantial and exceed values of $(N_b(\mathrm{CH})–N_\infty(\mathrm{CH}))/N_\infty(\mathrm{CH}) \geq 2$.

The present data for HD 54662 in CMa OB1 are very consistent with the earlier results of Paper I. The saturation corrections obtained for b(CH) of 1.5 km s^{-1} are small and do not exceed 10%. For the stars in CMa OB1, the values N_b(CH) as listed in Paper I are adopted as final CH column densities in the discussion of Sects. 4.2 and 4.3.

Toward HD 63423 and HD 62150, the present CH measurements agree very well with the COG analysis of Paper I. Toward HD 61827, HD 62844, and CPD−33°1768, the CH column densities inferred here are larger than N_∞(CH) but lower than N_b(CH) of Paper I. This suggests CH Doppler parameters greater than 1.5 km s^{-1}. For the three stars, we obtain final CH column densities which are lower by some 20–25% compared to the values for N_b(CH) given in Paper I. Toward CPD−32°1734, the CH column density obtained here is lower than N_∞(CH) inferred from both the CAT and the EMMI measurements of Paper I. The present measurement is associated with a relatively large error of some 15%. We adopt a final column density of $N(\mathrm{CH}) = 9 \times 10^{13}$ cm^{-2} for CPD−32°1734.

Toward HD 74194, CPD−44°3129, and CPD−45°3218 in Vela OB1, CH column densities inferred here agree with those of Paper I obtained with b(CH) = 1.5 km s^{-1}. Toward HD 75149, HD 75211, HD 76556, and CPD−46°3272, the CH column densities are some 10% lower than those of Paper I. Toward HD 75860, we adopt a value of $N(\mathrm{CH}) = 2.8 \times 10^{13}$ cm^{-2} which is some 20% lower than that given in Paper I, and $N(\mathrm{CH}) = 6 \times 10^{13}$ cm^{-2} for HD 78344. The CH column densities toward HD 114886, HD 112366, HD 115363, HD 112272, and HD 114213 in Cen OB1 derived here agree with those obtained with b(CH) = 1.5 km s^{-1}. Toward HD 110639, HD 113432, and HD 113422, the column densities obtained here are lower than the values N_∞(CH) of Paper I; this may reflect measurement uncertainties to a large extent. We use the averages obtained in the limit of $b \rightarrow \infty$ as final CH column densities toward the latter stars. Toward HD 114011, the saturation corrections of Paper I are probably too high as well. The column densities derived here and in Paper I in the limit of unsaturated lines agree, and we proceed to use the average obtained in the limit of b(CH)$\rightarrow \infty$ as the final CH column density toward this star.

4. Discussion

Revised CH column densities obtained in Sect. 3.2 and final CN column densities obtained from the various methods discussed in Sect. 3.1 are summarised in Cols. 2 and 4, respectively, of Tables 7 and 8. For completeness, we add measured CH^+ and C_2 column densities of Gredel (1997) and Gredel (1999) in Cols. 3 and 5, respectively, as well as the results for CMa OB1 and NGC 4755 from these papers. Heliocentric velocities for CH, CH^+, CN, and C_2 absorption are given in Cols. 6–9, respectively. In Col. 10 of these tables, we list the velocity of CO emission most likely associated with the molecular absorption. Tables 7 and 8 provide a coherent set of measurements of diatomic molecules toward the CMa OB1, NGC 2439, Vela OB1, NGC 4755, and Cen OB1 associations.

4.1. Radial velocities of CN, C_2, CH, and CH^+

In general, the measured radial velocities of CN agree well with those of CH, CH^+, C_2, and CO. Exceptions occur toward HD 75211 and CPD−44°3129, where the CN radial velocity differs by some 6 and 4 km s^{-1}, respectively, from that of the other molecules. The CN absorption lines toward HD 110639, HD 113432, and HD 114213 are resolved into two well separated components, and those toward HD 61827 are partially resolved. With the exception of HD 61827, the CH^+ and CH absorption lines toward these stars are also resolved into two absorption components with similar heliocentric velocities. The CH and CH^+ lines in the spectrum of HD 61827 are relatively broad, with velocities that correspond to the average velocity of the two CN components. The C_2 absorption lines toward HD 61827 are partly resolved into two components as well, and those toward HD 113422 and HD 113432 are resolved into two components. In all cases, the C_2 radial velocities are similar to those of CN (Gredel 1999).

The CH radial velocities derived in Sect. 2.3 are generally in very good agreement with the measurements of

Table 7. Final CH, CH^+, CN, and C_2 data for CMa OB1, NGC 2439, and Vela OB1.

star	N(CH)	N(CH^+)	N(CN)	N(C_2)	$V_{\rm hel}$(CH)	$V_{\rm hel}$(CH^+)	$V_{\rm hel}$(CN)	$V_{\rm hel}$(C_2)	$V_{\rm hel}$(CO)
	10^{13} cm^{-2}				km s^{-1}				
CMa OB1									
HD 55879	≤0.1	0.35(0.10)	-	-	24:	23.8	-	-	24:
HD 53975	<0.2	0.3(0.2)	-	-	33:	33.4	-	-	33:
HD 53755	0.3(0.2)	0.9(0.2)	-	-	26.9	29.8	-	-	35.0
HD 54662	0.8(0.1)	1.1(0.1)	-	-	35.8	35.5	-	-	32.6
HD 52382	1.1(0.1)	2.4(0.2)	-	-	36.0	37.2	-	-	37.7
NGC 2439									
HD 63423	3.5(0.2)	1.1(0.2)	$1.25^{+0.45}_{-0.25}$	-	40.5	39.4	41.1	-	40.6–41.4
HD 62150	2.4(0.1)	2.9(0.3)	0.05(0.03)	-	38.4	39.8	37.8	-	36.7
HD 61827	2.6(0.1)	1.3(0.1)[a]	0.36(0.07)	2.8(0.5)	36.3	38.3[a]	35.4	36.8	34.9
	1.5(0.1)	–[a]	0.36(0.07)	3.8(0.5)	41.7	–[a]	41.4	43.4	41.0
HD 62844	5.0(0.5)	3.2(0.2)	0.31(0.06)	-	39.1	39.7	38.1	-	39:
CPD−32°1734	9.0(2.0)	6.0(0.5)	1.0(0.2)	10.5(1.0)	37.8	37.8	38.7	37.8	38.3
CPD−33°1768	12.0(3.0)	4.4(0.5)	0.95(0.10)	11.0(1.5)	38.6	43.3	40.6	41.5	39.7
HD 63804[b]	5.3(0.8)	4.8(0.3)	$2.9^{+5.0}_{-1.5}$	10.0(4.0)	37.7	37.2	37.6	39.5	37.0
Vela OB1									
HD 78344	6.0(0.5)	3.5(0.4)	2.67(0.50)	-	19.5	20.9	20.2	-	19.6–21.4
HD 74371	1.0(0.1)	1.4(0.2)	<0.05	-	22.8	23.5	23:	-	23:
HD 75149	1.7(0.2)	1.2(0.1)	0.07(0.02)	<0.5	24.2	24.2	22.4	22:	22:
HD 74194	1.3(0.1)	1.7(0.5)	<0.05	-	22.1	20.0	22:	-	22:
HD 75211	2.3(0.2)	3.6(0.2)	0.33(0.04)	-	24.1	24.3	18.1	-	18.1–22.5
HD 76556	4.0(0.5)	1.5(0.2)	1.18(0.20)	-	19.9	4.0[d]	19.0	-	19.7
HD 75860	2.8(0.3)	7.5(0.5)	<0.05	<0.5	20.9	21.6	21:	21:	18.7–23.7
CPD−44°3129	5.3(0.5)	6.3(1.5)	0.78(0.10)	3.3(1.5)	21.3	22.8	18.0	21.9	18.7–21.2
CPD−45°3218	9.0(2.0)	2.8(0.5)	4.0(1.0)[e]	-	22.0	22.1	21.7	-	20.2–22.7
CPD−46°3272	6.0(1.0)	3.2(0.5)	1.4(0.1)[e]	6.0(1.5)	21.3	22.1	22.0	21.4	19.7–23.3
HD 73882[b]	3.7(0.5)	2.4(0.3)	3.8(0.4)	3.5(1.0)	21.3	21.5	21.3	21.8	22.6

[a] Unresolved; 2 velocity components seen in CH, CN, C_2, CO.
[b] From Gredel et al. (1993), rescaled to $f_{\rm abs}$ used here.
[c] Possibly affected by flexure from EMMI.
[d] Possible error in data reduction (see text).
[e] See text.

Gredel (1997). An exception occurs toward HD 76556, where our present value for $V_{\rm hel}$(CH) of 19.9 km s^{-1} is in clear contrast to the earlier value of 1.9 km s^{-1}. Because the velocity inferred here agrees with that of CN, $V_{\rm hel}$(CN) = 19 km s^{-1}, and because these velocities are similar to CH and CN radial velocities of other stars in Vela OB1, we suspect that the CH velocity given by Gredel (1997) toward HD 76556 is wrong. Possibly, the CH^+ velocity of $V_{\rm hel}$ = +4 km s^{-1} toward that star is wrong as well, and we disregard the data toward HD 76556 in the following discussion.

Figure 6 contains a plot of the velocity differences V(CN)–V(CH), V(CN)–V(CH^+), V(CN)–V(C_2), and V(CN)–V(CO) versus the velocity of CN obtained from the final heliocentric velocities given in Tables 7, 8. In cases where ranges of velocities for CO are given, the central value is adopted as CO velocity. The scatter of some 1.5 km s^{-1} in the velocity differences reflect the uncertainties in the derived heliocentric velocities. Apart from two stars in Vela OB1, where the velocity of CN differs significantly from that of the other molecules, the velocity of CH^+ toward HD 113432 differs by 3.5–4 km s^{-1} from the velocity of CN and that of the other observed molecules. Toward all other sightlines studied here, the radial velocities of CN, CH, C_2, CO, and CH^+ agree within the errors. In cases where the CO velocities are spread over a range of velocities, the central CO velocities is used.

It has been debated in the past whether or not the velocities of the CH^+ lines show systematic shifts with respect to the velocities of lines from neutrals such as CH, CN, or C_2. Velocity shifts up to a few km s^{-1} between CH^+ and CH were suggested by models which

Table 8. Final CH, CH^+, CN, and C_2 data for NGC 4755 and Cen OB1.

star	N(CH)	N(CH^+)	N(CN)	N(C_2)	$V_{\rm hel}$(CH)	$V_{\rm hel}$(CH^+)	$V_{\rm hel}$(CN)	$V_{\rm hel}$(C_2)	$V_{\rm hel}$(CO)
	10^{13} cm^{-2}				km s^{-1}				
NGC 4755									
HD 111973	0.3(0.1)	0.4(0.1)	-	<0.5	−10.6	−13.3	-	−12:	
	0.5(0.1)	0.9(0.1)	-	<0.5	7.8	8.6	-	8:	
HD 111904	0.3(0.1)	0.7(0.1)	-	-	−13.0	−12.6			
	0.4(0.1)	0.5(0.1)	-	-	8.2	8.6			
HD 111934	0.4(0.1)	0.6(0.1)	-	-	−10.6	−11.9			
	0.5(0.1)	0.6(0.1)	-	-	8.2	8.6			
HD 111990	0.4(0.1)	0.9(0.1)	-	-	−10.6	−14.0			
	0.7(0.1)	0.6(0.1)	-	-	8.2	7.9			
CPD−59°4551	0.7(0.2)	1.8(0.1)	-	-	−11.2	−11.2			
	0.7(0.2)	0.9(0.1)	-	-	8.2	7.2			
Cen OB1									
HD 114886	0.4(0.1)	0.6(0.1)	-	-	−21.8	−20.4	-	-	-
	0.5(0.2)	1.4(0.1)	-	-	4.1	2.3	-	-	-
HD 115704	1.3(0.1)	2.3(0.2)	-	-	−28.0	−25.1	-	-	−30.5
	0.5(0.1)	0.5(0.2)	-	-	1.2	2.6	-	-	2:
HD 112366	<0.4	1.3(0.2)	-	-	−14:	−13.9	-	-	−10.8–−18.4
	3.8(0.5)	0.8(0.1)	1.90(0.20)	-	5.3	4.3	5.4	-	6.2
HD 115363	1.1(0.1)	0.9(0.2)	<0.05	-	−22.5	−20.4	−22:	-	−22.0
	2.5(0.2)	0.9(0.2)	0.28(0.02)	-	4.2	4.4	3.8	-	4.3
HD 110639	2.0(0.2)	1.2(0.1)	0.16(0.05)	<0.5	−20.3	−19.6	−20.6	−20.5:	−20.5
	1.4(0.1)	2.4(0.2)	0.57(0.05)	<0.5	3.9	4.4	2.9	3.5:	3.5
HD 114011	4.7(0.4)	2.0(0.4)	3.79(0.40)	7.5(1.0)	−25.9	−23.9	−24.9	−26.4	−24.7
	<0.5	0.6(0.1)	-	<0.5	4:	0.1	-	4:	4:
HD 113432	1.1(0.2)	2.2(0.4)	-	1.2:	−17.6	−19.0	-	−15.2:	−18.3
	3.7(0.2)	1.4(0.4)	1.88(0.30)	1.6:	4.1	0.9	4.7	4.6:	2.4–3.6
HD 113422	2.6(0.3)	4.0(0.3)	0.32(0.05)	3.0(1.0)	−18.2	−18.2	−18.5	−17.8	−18.8
	1.6(0.2)	1.6(0.2)	0.44(0.10)	<0.8	3.4	3.7	3.2	2.7:	3.4
HD 112272	2.8(0.2)	2.5(0.3)	-	-	−8.2	−7.1	-	-	−10.2
	2.8(0.2)	1.3(0.2)	0.18(0.04)	-	4.0	6.1	5.0	-	5.3
HD 114213	4.1(0.3)	1.3(0.4)	4.68(1.00)	3.5(0.5)	−20.0	−20.4	−20.0	−20.8	−19.6
	1.8(0.8)	<0.5	0.28(0.08)	<0.5	2.4	2.4:	3.2	3.6:	3.6

attempted to explain CH^+ formation in magnetic hydrodynamic shocks (Pineau des Forêts et al. 1986). Flower & Pineau des Forêts (1998) have eased the earlier constraints and purported a way in which the CH^+ velocity can be brought in agreement with that of CH. The reaction rates adopted by Flower & Pineau des Forêts (1998) imply that CH is efficiently removed in the cool gas, and that significant fractions of interstellar CH form in the hot post-shock gas as well (c.f. discussion in Gredel 1999), at elevated temperatures of many 100 K; this material is rich in CH^+. However, the empirically established, tight correlation between the CH and C_2 column densities (Federman et al. 1994; Gredel 1999), together with the very low gas-kinetic temperatures of a few ten K derived from C_2 excitation (Gredel 1999), is difficult to explain in terms of a significant formation of CH in hot material. The ultra-high resolution observations of Lambert et al. (1990) and others show that the CH line profile may be described in terms of a CH^+-like component, with rather large width, and a CN-like component, with a narrow width. Gredel (1999) estimated an upper limit of some 20% of CH in CH^+-like gas toward the southern associations. In Sect. 4.3, we introduce an ad hoc component of some 10–50 criss-crossing MHD shocks where the amount of CH^+-like CH is restricted to observe this limit.

4.2. Chemistry of CN in quiescent gas

We extracted gas densities, $n = 2n(H_2) + n(H)$, from the observational results on CN presented in Tables 7 and 8 in conjunction with those on CH and C_2 (when the latter were available) with an updated version of the chemical model described by Federman et al. (1994). The updates, which were needed to keep reaction rates the same as before when using current values for the abundance of C^+ (Sofia et al. 1997), are discussed in detail elsewhere (Knauth et al. 2001; Pan et al. 2001). The synthesis of CN along the sight lines studied here arises from N reacting with CH and C_2, while the production of C_2 is initiated by the reaction $C^+ + CH \rightarrow C_2^+ + H$. The main destruction pathways for CN and C_2 are photodissociation

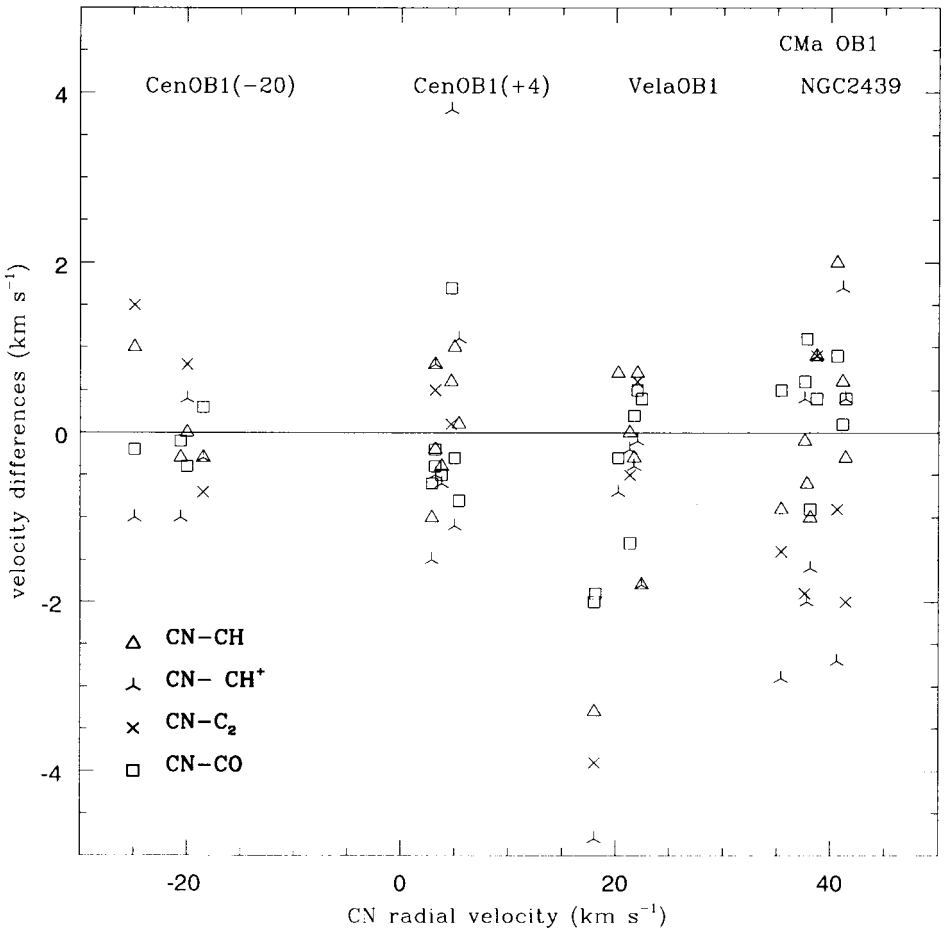

Fig. 6. Velocity differences V(CN)–V(CH), V(CN)–$V(CH^+)$, V(CN)–$V(C_2)$, and V(CN)–V(CO) plotted versus the velocity of CN.

and reactions with atomic O and N, the latter being relevant for C_2. The parameter α, which is used to estimate the conversion of C^+ into CO as the extinction within a cloud increases, is especially important for these reddened sight lines; it is given by $[1 + 14(\tau_{UV} - 2)/5]^{-1}$. The determination of $N(C_2)$ is based on the observed amount of CH and that of N(CN) on the observed amounts of CH and C_2. For sight lines without measurements on C_2, the predicted amount of C_2 is used in the derivation for N(CN).

The calculations proceeded under the following conditions. The kinetic temperature for all clouds was set to 50 K, but we note that the results are not very sensitive to its value. The fractional abundances for C^+, N, and O in unshielded regions were 1.4×10^{-4} (Sofia et al. 1997), 7.5×10^{-5} (Meyer et al. 1997), and 3.2×10^{-4} (Meyer et al. 1998), respectively. The value for τ_{UV} was set equal to $2A_V$ (Federman et al. 1994), but for directions with 2 absorption components separated by at least 20 km s^{-1}, each component was assumed to have half the total extinction for the line of sight. Density estimates were obtained for models with a UV flux equal to the average interstellar value ($I_{UV} = 1$) and with a flux that is a factor of 5 stronger. Since a factor-of-5 increase in the UV flux is expected to increase the abundance of C^+ (at the expense of CO) for moderately reddened directions, the model had to accommodate this possibility. For sight lines with τ_{UV} greater than 4, the factor-of-5 increase in flux was accomplished by decreasing τ_{UV} by 1.61 so that α remained closer to 1. Finally, since the chemical scheme pertains to diffuse molecular clouds, models with densities greater than 1600 cm^{-3} were not considered.

The results of our analysis appear in Tables 9 and 10. Densities typical of diffuse molecular gas (100 to 1400 cm^{-3}) are obtained for most of the sightlines in our study, usually for both choices of enhancement factor in the UV flux. Lower limits of 1600 cm^{-3} are inferred toward CPD−32°1734 and CPD−33°1768, indicating that CN is mainly produced under dark cloud conditions. The same seems to apply for the gas toward HD 114011, where the results based on a density of 1600 cm^{-3} are lower than the observed CN and C_2 columns, but within their uncertainties. Dark cloud chemistry also appears to be operating when the model can reproduce the C_2 column, but falls short for CN, such as toward HD 73882, HD 110639 at +3 km s^{-1}, HD 113432, HD 113422 at +3 km s^{-1}, and HD 114213 at −20 km s^{-1}. For sightlines with upper limits on the column of CN [HD 74371, HD 74194, HD 75860, and HD 115363(−22)], the densities are found to be less than about 200 cm^{-3} (for I_{UV} of 1). Since C_2 absorption is

Table 9. Chemical analysis for gas toward NGC 2439 and Vel OB1.

star	τ_{UV}	n (cm^{-3})		$N(C_2)$ (10^{13} cm^{-2})			N(CN) (10^{13} cm^{-2})		
		$I_{UV}=1$	$I_{UV}=5$	Observed	$I_{UV}=1$	$I_{UV}=5$	Observed	$I_{UV}=1$	$I_{UV}=5$
NGC 2439									
HD 63423	3.06	1325	>1600	...	5.2	...	$1.25^{+0.45}_{-0.25}$	1.25	...
HD 62150	3.54	50	250	...	0.3	0.3	0.05(0.03)	0.05	0.05
HD 61827(+35)	4.20	200	600	2.8(0.5)	1.3	2.4	0.36(0.07)	0.42	0.40
HD 61827(+41)	4.20	250	925	3.8(0.5)	0.9	2.0	0.36(0.07)	0.42	0.43
HD 62844	5.34	30	125	...	1.0	1.5	0.31(0.06)	0.27	0.29
CPD−32°1734	7.32	...	>1600	10.5(0.5)	...	...	1.0(0.2)	...	...
CPD−33°1768	8.76	...	>1600	11.0(1.5)	...	...	0.95(0.10)	...	...
HD 63804	7.14	175	750	10.0(4.0)	3.9	5.4	$2.9^{+5.0}_{-1.5}$	3.4	3.4
Vela OB1									
HD 78344	8.40	150	275	...	4.0	4.8	2.67(0.50)	2.66	2.67
HD 74371	1.86	<225	<1075	...	<0.5	<0.5	<0.05	<0.05	<0.05
HD 75149	2.28	175	825	<0.5	0.6	0.6	0.07(0.02)	0.07	0.06
HD 74194	3.24	<125	<575	...	<0.3	<0.3	<0.05	<0.05	<0.05
HD 75211	4.32	200	575	...	1.2	2.0	0.33(0.04)	0.33	0.34
HD 76556	4.38	475	1175	...	3.6	5.8	1.18(0.20)	1.16	1.19
HD 75860	5.58	<20	<30	<0.5	<0.4	<0.3	<0.05	<0.13	<0.05
CPD−44°3129	6.20	40	150	3.3(1.5)	2.0	2.5	0.78(0.10)	0.83	0.75
CPD−45°3218	6.36	350	825	...	7.7	10.0	4.0(1.0)	4.0	4.0
CPD−46°3272	6.36	70	275	6.0(1.5)	3.2	4.3	1.4(0.1)	1.7	1.6
HD 73882	4.32	875	...	3.5(1.0)	4.3	...	3.8(0.4)	1.4	...

Table 10. Chemical analysis for gas toward Cen OB1.

star	τ_{UV}	n (cm^{-3})		$N(C_2)$ (10^{13} cm^{-2})			N(CN) (10^{13} cm^{-2})		
		$I_{UV}=1$	$I_{UV}=5$	Observed	$I_{UV}=1$	$I_{UV}=5$	Observed	$I_{UV}=1$	$I_{UV}=5$
Cen OB1									
HD 112366	4.50	1250	>1600	...	4.8	...	1.90(0.20)	1.91	...
HD 115363(−22)	2.58[a]	<200	<975	...	<0.4	<0.4	<0.05	<0.05	<0.05
HD 115363(+4)	2.58[a]	500	>1600	...	2.0	...	0.28(0.02)	0.3	...
HD 110639(−21)	2.73[a]	175	850	<0.5	0.6	0.6	0.16(0.05)	0.09	0.08
HD 110639(+3)	2.73[a]	225	1150	<0.5	0.5	0.6	0.57(0.05)	0.08	0.08
HD 114011	5.88	>1600	>1600	7.5(1.0)	...	6.5	3.79(0.40)	...	2.67
HD 113432	6.12	80	175	1.6:	2.0	1.9	1.88(0.30)	0.77	0.51
HD 113422(−19)	3.24[a]	375	>1600	3.0(1.0)	1.7	...	0.32(0.03)	0.38	...
HD 113422(+3)	3.24[a]	275	1400	<0.8	0.8	0.8	0.44(0.10)	0.15	0.15
HD 112272(+5)	6.54	...	50	...	...	0.7	0.18(0.04)	...	0.18
HD 114213(−20)	3.42[a]	675	>1600	3.5(0.5)	4.0	...	4.68(1.00)	0.93	...
HD 114213(+3)	3.42[a]	175	825	<0.5	0.6	0.6	0.28(0.08)	0.11	0.11

[a] Each component has 1/2 the extinction along the line of sight.

not observed for any of these sightlines either, the amount of CH is probably controlled by the synthesis of CH^+ in relatively low density gas. Ellipses in Tables 9 and 10 are given where the modeling results cannot be determined under the circumstances. One concern remains when analyzing these data: how much of the extinction in these reddened sight lines comes from the molecule-rich gas? Unfortunately, no measures of H I content are available, and so we had to assume that the extinction arose from one cloud (unless there were distinct velocity components separated by more than 20 $km\,s^{-1}$). Use of lower extinctions per cloud would result in higher inferred densities because photodissociation would play a more important role. The inferred densities are in excellent agreement with densities inferred from C_2 excitation (Gredel et al. 1993; Gredel 1999).

4.3. CH^+ production in MHD shocks

The formation of CH^+ in translucent clouds has been studied by many authors involving different scenarios with mixed success: MHD shocks (Draine & Katz 1986; Pineau des Forêts et al. 1986), turbulent boundary layers (Duley et al. 1992), non-maxwellian velocity distributions (Spaans 1995) or interstellar turbulence

(Falgarone et al. 1995; Joulain et al. 1998). All these processes have been reviewed in the context of CH^+ formation by Gredel (1997). In practice, these models have difficulties in reproducing, all together, the observational constraints: (1) the correlation between the column density $N(CH^+)$ and that of rotationally excited H_2, (2) the trend of $N(CH^+)$ with visual extinction of the background star and with CH column density, and (3) the absence of a significant CH-CH^+ velocity shift. Furthermore, the observations show that this velocity shift does not increase with CH^+ column density. The purpose of the present approach is to provide a model consistent with these different constraints.

Flower & Pineau des Forêts (1998) calculated CH and CH^+ line profiles in C-type shocks and showed that the predicted velocity shift is much smaller than had been assumed previously. CH is formed via dissociative recombination, CH_3^+(e, H_2)CH, at the ion flow speed but is rapidly destroyed through the reaction CH(H, H_2)C before being thermalized by collisions with the neutrals, leading to a velocity of CH close to the ion (CH^+) speed. A single C-shock along a given line of sight could then explain most of the observed CH^+ column densities. The scaling relation between observed CH^+ column density and visual extinction is approximately $N(CH^+) = 10^{13} \times A_V$ cm^{-2}; it could be explained by one C-shock with a velocity of 12 km s^{-1} leading to a predicted velocity shift between CH^+ and CH of less than 2 km s^{-1}. However, as proposed by Gredel (1997), it is more likely that several shock waves will be present along the line of sight, with lower velocities, and that the number correlates with the optical depth of the clouds.

We considered a model of MHD shocks that was described by Flower & Pineau des Forêts (1998). We extended the chemical network to 97 chemical species containing H, He, C, N, O, S and a representative metal linked by approximately 800 chemical reactions. The initial elemental abundances were taken from Meyer (1997). To illustrate the dissipation of kinetic energy through a number of low velocity shocks along the lines of sight, we used only two C-shock models with velocities of 8 and 9 km s^{-1} propagating into a preshock gas of density $n = 20$ cm^{-3} in which the transverse magnetic induction is assumed to be 5 μG.

The preshock gas is supposed to be at steady state, at a temperature of 80 K, and illuminated by the standard local interstellar radiation field. To calculate the preshock abundances of the species, we used an updated version of the Photon Dominated Region (PDR) model of Le Bourlot et al. (1993). For a visual extinction A_V= 0.1, the model yields an H_2/H ratio in the preshock gas of approximately 0.15. H_2 and CO photodissociation rates from the PDR model are expressed as functions of A_V and then are introduced into the shock model. A more detailed description of the shock model and of the main chemical reactions involved can be found in Flower & Pineau des Forêts (1998).

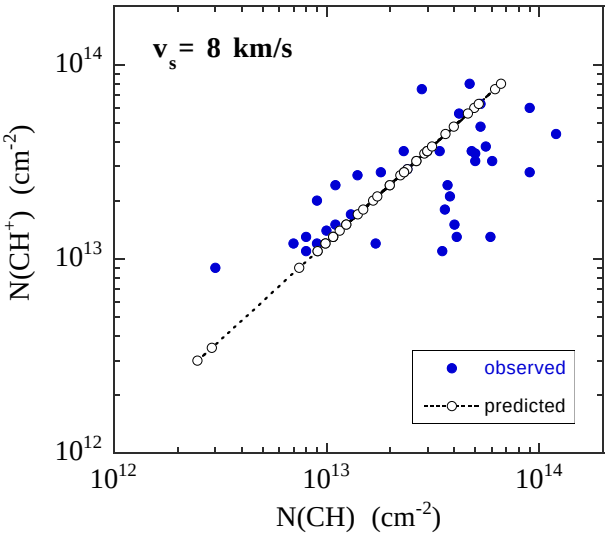

Fig. 7. CH^+ versus CH column densities in shocks of V_s = 8 km s^{-1}.

We calculated the number of shocks necessary to reproduce the observed CH^+ column density toward the different lines of sight. Tables 11 and 12 contain the resulting CH and CH^+ column densities. Columns 1 and 2 contain the star and the total visual extinction along the line of sight. Columns 3 and 4 give the fraction of gas (in units of A_V) in the MHD component. The fraction of gas in the shocked gas varies from sightline to sightline and with the velocities of the shocks, but the total amount of gas in the hot component is small in all cases. Columns 5 and 6 give the number of shocks per sightline, N_s, for shock velocities V_s of 8 and 9 km s^{-1}, respectively.

The observed CH and CH^+ column densities are given in Cols. 7 and 10. Columns 8 and 9 contain the column density of CH produced in shocks of 8 and 9 km s^{-1}, respectively, and Cols. 11 and 12 that of CH^+. The number of shocks toward each line of sight is chosen to reproduce the observed CH^+ column densities. The amount of CH^+-like CH, that is, the amount of CH produced in the MHD shocks, is very large for low shock velocities ($V_s \leq 7$ km s^{-1}). This is illustrated in Figs. 7 and 8, where the predictions of the models, varying the number of shocks, are compared to the observations. For lower shock velocities, there are a greater number of shocks along the line of sight, with larger CH column densities (i.e. the $N(CH)/N(CH^+)$ ratio). The consequence is that for lower velocities (i.e. 6 or 7 km s^{-1}) too much CH is produced in the MHD component, unless the magnetic field is reduced. For shock speeds above 8 km s^{-1}, a fraction of 10–30% of CH^+-like CH is obtained in general.

As is demonstrated in Figs. 9 and 10, N_s is well distributed around 20 shocks of velocity 8 km s^{-1} per A_V and 5 shocks of velocity 9 km s^{-1} per A_V respectively. We emphasise that this approach is only an illustration and a mixture of shocks with various velocities (and directions) may be present along the different lines of sight. It is nevertheless obvious that the number N_s varies from one line

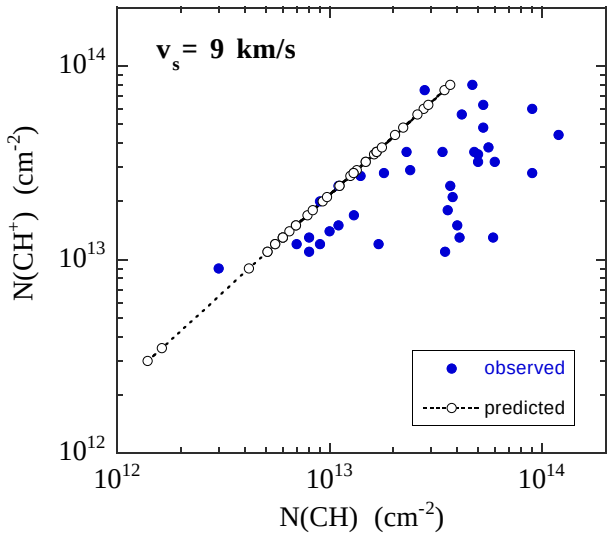

Fig. 8. CH^+ versus CH column densities in shocks of V_s = 9 km s^{-1}.

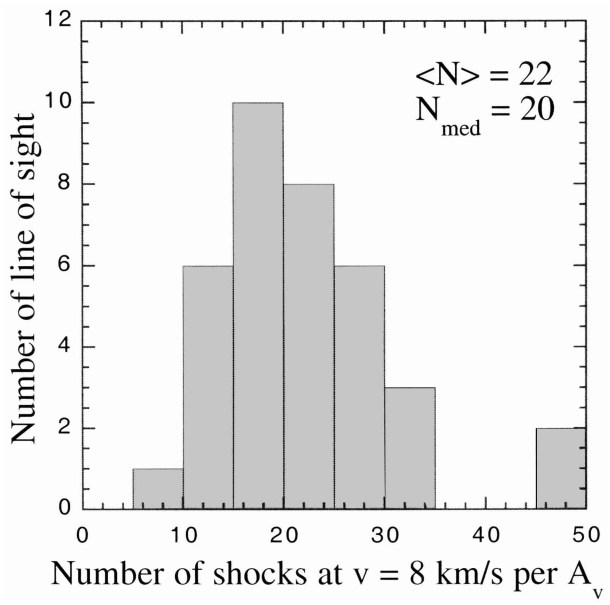

Fig. 9. Number of shocks per sightline for V_s = 8 km s^{-1} required in model to reproduce observed column densities of CH^+.

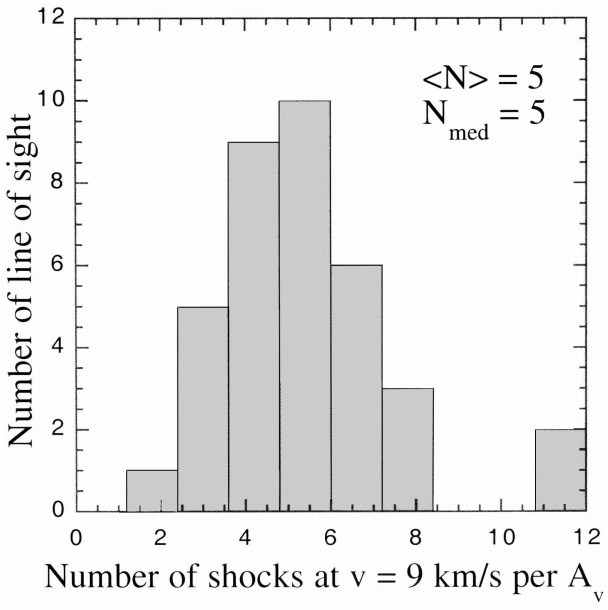

Fig. 10. Number of shocks per sightline for V_s = 9 km s^{-1} required in model to reproduce observed column densities of CH^+.

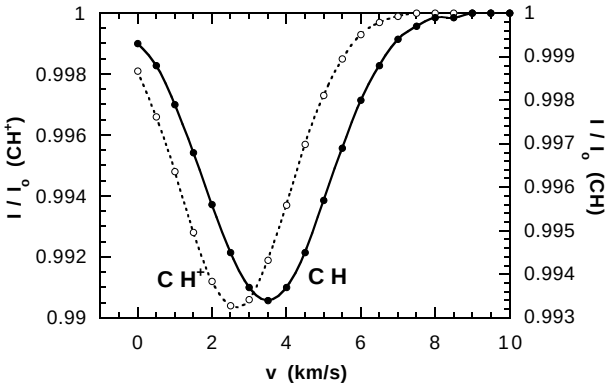

Fig. 11. CH and CH^+ absorption line profiles in an 8 km s^{-1} MHD shock.

of sight to another and is not, then, an "interstellar constant".

We also give in Tables 11 and 12 the predicted columns of CO and OH in Cols. 13–16, again for shock speeds of 8 and 9 km s^{-1}. Observational confirmation of these predicted column densities would be an important test of the present model. The amount of CN and C_2 produced in the shocks is very low and stays below column densities of 10^{12} cm^{-2} in all cases.

As an illustration, the computed absorption line profiles for CH and CH^+ in a single shock of velocity 8 km s^{-1} (using a microturbulent velocity b = 2 km s^{-1}) are presented in Fig. 11 where velocities are expressed in the shock frame. It is clear that even for a shock propagating along the line of sight, the velocity shift between CH and CH^+ is smaller than 1 km s^{-1}. Furthermore, for shocks propagating in random directions along the line of sight, the effect of projection reduces the kinematic broadening (and hence the width of the CH line relative to that of CH^+), as well as the shift between CH and CH^+ (Flower & Pineau des Forêts 1998).

When some of the CH arises from MHD shocks, less of the observed CH column comes from the quiescent gas. We investigated the effect of reduced CH column by subtracting the amount of CH^+-like CH produced by 9 km s^{-1} shocks (cf. Col. 9 of Tables 11 and 12) from the total observed CH column density and iterating the analysis of Sect. 4.2. Generally, when C_2 and CN photodissociation dominate, the inferred densities given in Tables 9 and 10 scale inversely with N(CH); a larger n is needed to compensate for a reduced N(CH). This situation applies to

Table 11. Modeled CH, CH^+, CO, and OH column densities in the hot MHD component toward CMa OB1, NGC 2439, and Vel OB1.

star	A_V(mag)			N_s		N(CH)			$N(CH^+)$			N(CO)		N(OH)	
						10^{13} cm^{-2}			10^{13} cm^{-2}			10^{13} cm^{-2}		10^{13} cm^{-2}	
HD/CPD	tot	S8	S9	S8	S9	obs	S8	S9	obs	S8	S9	S8	S9	S8	S9
55879	0.36	0.07	0.01	16	4	0.0	0.3	0.1	0.3	0.4	0.2	1.7	0.7	1.3	0.5
53975	0.66	0.06	0.01	8	2	0.0	0.2	0.1	0.3	0.3	0.2	1.4	0.7	1.0	0.5
53755	0.75	0.18	0.04	20	5	0.3	0.7	0.4	0.9	0.9	1.0	4.2	2.7	3.1	2.1
54662	1.05	0.21	0.04	18	4	0.8	0.9	0.4	1.1	1.1	1.0	5.0	2.7	3.8	2.1
52382	1.32	0.48	0.10	31	8	1.1	2.0	1.1	2.4	2.4	2.4	11.2	6.7	8.4	5.3
63423	1.53	0.21	0.04	12	3	3.5	0.9	0.4	1.1	1.1	1.0	5.0	2.7	3.8	2.1
62150	1.77	0.58	0.11	28	7	2.4	2.4	1.3	2.9	2.9	2.9	13.7	8.1	10.2	6.4
61827	2.10	0.26	0.05	10	3	4.1	1.1	0.6	1.3	1.3	1.2	6.1	3.4	4.6	2.7
62844	2.67	0.64	0.12	20	5	5.0	2.6	1.5	3.2	3.2	3.1	15.1	8.7	11.3	6.9
−32°1734	3.66	1.20	0.24	28	7	9.0	4.9	2.8	6.0	6.0	6.0	28.2	16.8	21.1	13.3
−33°1768	4.40	0.88	0.17	17	4	12.0	3.6	2.0	4.4	4.4	4.4	20.6	12.1	15.5	9.6
63804	3.36	0.96	0.19	24	6	5.3	4.0	2.2	4.8	4.8	4.8	22.6	13.4	16.9	10.6
78344	4.20	0.70	0.13	14	3	5.0	2.9	1.6	3.5	3.5	3.4	16.5	9.4	12.3	7.4
74371	0.93	0.29	0.06	25	6	1.0	1.2	0.7	1.4	1.4	1.5	6.7	4.0	5.0	3.2
75149	1.14	0.24	0.05	18	4	1.7	1.0	0.6	1.2	1.2	1.2	5.6	3.4	4.2	2.7
74194	1.62	0.34	0.07	18	4	1.3	1.4	0.8	1.7	1.7	1.7	8.1	4.7	6.1	3.7
75211	2.16	0.73	0.14	28	7	2.3	3.0	1.7	3.6	3.6	3.6	17.0	10.1	12.7	8.0
76556	2.19	0.30	0.06	12	3	4.0	1.2	0.7	1.5	1.5	1.5	7.0	4.0	5.2	3.2
75860	2.79	1.50	0.30	45	11	2.8	6.2	3.5	7.5	7.5	7.5	35.2	20.8	26.3	16.5
−44°3129	3.10	1.26	0.25	34	8	5.3	5.2	2.9	6.3	6.3	6.3	29.6	17.5	22.2	13.8
−45°3218	3.18	0.56	0.11	15	4	9.0	2.3	1.3	2.8	2.8	2.9	13.1	8.1	9.8	6.4
−46°3272	3.18	0.64	0.12	17	4	6.0	2.6	1.5	3.2	3.2	3.1	15.1	8.7	11.3	6.9
73882	2.13	0.48	0.10	19	5	3.7	2.0	1.1	2.4	2.4	2.4	11.2	6.7	8.4	5.3

Table 12. Modeled CH, CH^+, CO, and OH column densities in the hot MHD component toward NGC 4755 and Cen OB1.

star	A_V(mag)			N_s		N(CH)			$N(CH^+)$			N(CO)		N(OH)	
						10^{13} cm^{-2}			10^{13} cm^{-2}			10^{13} cm^{-2}		10^{13} cm^{-2}	
HD/CPD	tot	S8	S9	S8	S9	obs	S8	S9	obs	S8	S9	S8	S9	S8	S9
111973	1.00	0.26	0.05	22	5	0.8	1.1	0.6	1.3	1.3	1.2	6.1	3.4	4.6	2.7
111904	1.00	0.24	0.05	20	5	0.7	1.0	0.6	1.2	1.2	1.2	5.6	3.4	4.2	2.7
111934	1.08	0.24	0.05	19	5	0.9	1.0	0.6	1.2	1.2	1.2	5.6	3.4	4.2	2.7
111990	1.16	0.30	0.06	22	5	1.1	1.2	0.7	1.5	1.5	1.5	7.0	4.0	5.2	3.2
−59°4551	1.40	0.54	0.11	32	8	1.4	2.2	1.2	2.7	2.7	2.7	12.6	7.4	9.4	5.8
114886	1.28	0.40	0.08	26	6	0.9	1.7	0.9	2.0	2.0	1.9	9.5	5.4	7.1	4.2
115704	2.22	0.56	0.11	21	5	1.8	2.3	1.3	2.8	2.8	2.9	13.1	8.1	9.8	6.4
112366	2.24	0.42	0.09	16	4	3.8	1.7	1.0	2.1	2.1	2.2	9.8	6.0	7.3	4.8
115363	2.58	0.36	0.07	12	3	3.6	1.5	0.8	1.8	1.8	1.7	8.4	4.7	6.3	3.7
110639	2.74	0.73	0.14	22	5	3.4	3.0	1.7	3.6	3.6	3.6	17.0	10.1	12.7	8.0
114011	2.90	1.61	0.32	46	11	4.7	6.6	3.7	8.0	8.0	8.0	37.7	22.2	28.2	17.5
113432	3.06	0.73	0.14	20	5	4.8	3.0	1.7	3.6	3.6	3.6	17.0	10.1	12.7	8.0
113422	3.24	1.12	0.22	29	7	4.2	4.6	2.6	5.6	5.6	5.6	26.2	15.5	19.6	12.2
112272	3.26	0.76	0.15	20	5	5.6	3.1	1.8	3.8	3.8	3.9	17.9	10.8	13.4	8.5
114213	3.42	0.26	0.05	6	2	5.9	1.1	0.6	1.3	1.3	1.2	6.1	3.4	4.6	2.7

Table 13. Predicted columns for H_2 rotational levels in the shocked gas.

		$N(H_2)$ (cm^{-2}) V_s = 9 km s^{-1}						
star	A_V	$J=0$	$J=1$	$J=2$	$J=3$	$J=4$	$J=5$	$J=6$
HD 55879	0.36	1.3(18)	4.0(18)	2.2(17)	8.5(16)	2.4(15)	2.2(14)	1.5(12)
HD 53975	0.66	1.3(18)	4.0(18)	2.2(17)	8.5(16)	2.4(15)	2.2(14)	1.5(12)
HD 53755	0.75	5.2(18)	1.6(19)	8.9(17)	3.4(17)	9.7(15)	8.9(14)	6.0(12)
HD 54662	1.05	5.2(18)	1.6(19)	8.9(17)	3.4(17)	9.7(15)	8.9(14)	6.0(12)
HD 52382	1.32	1.3(19)	4.0(19)	2.2(18)	8.5(17)	2.4(16)	2.2(15)	1.5(13)
HD 63423	1.53	5.2(18)	1.6(19)	8.9(17)	3.4(17)	9.7(15)	8.9(14)	6.0(12)
HD 62150	1.77	1.5(19)	4.8(19)	2.7(18)	1.0(18)	2.9(16)	2.7(15)	1.8(13)
HD 61827	2.10	6.5(18)	2.0(19)	1.1(18)	4.2(17)	1.2(16)	1.1(15)	7.4(12)
HD 62844	2.67	1.7(19)	5.2(19)	2.9(18)	1.1(18)	3.2(16)	2.9(15)	1.9(13)
CPD−32°1734	3.66	3.2(19)	1.0(20)	5.5(18)	2.1(18)	6.1(16)	5.6(15)	3.7(13)
CPD−33°1768	4.40	2.3(19)	7.2(19)	4.0(18)	1.5(18)	4.4(16)	4.0(15)	2.7(13)
HD 63804	3.36	2.6(19)	8.0(19)	4.4(18)	1.7(18)	4.9(16)	4.5(15)	3.0(13)
HD 78344	4.20	1.8(19)	5.6(19)	3.1(18)	1.2(18)	3.4(16)	3.1(15)	2.1(13)
HD 74371	0.93	7.7(18)	2.4(19)	1.3(18)	5.1(17)	1.5(16)	1.3(15)	8.9(12)
HD 75149	1.14	6.5(18)	2.0(19)	1.1(18)	4.2(17)	1.2(16)	1.1(15)	7.4(12)
HD 74194	1.62	9.0(18)	2.8(19)	1.6(18)	5.9(17)	1.7(16)	1.6(15)	1.0(13)
HD 75211	2.16	1.9(19)	6.0(19)	3.3(18)	1.3(18)	3.6(16)	3.3(15)	2.2(13)
HD 76556	2.19	7.7(18)	2.4(19)	1.3(18)	5.1(17)	1.5(16)	1.3(15)	8.9(12)
HD 75860	2.79	4.0(19)	1.2(20)	6.9(18)	2.6(18)	7.5(16)	6.9(15)	4.6(13)
CPD−44°3129	3.10	3.4(19)	1.0(20)	5.8(18)	2.2(18)	6.3(16)	5.8(15)	3.9(13)
CPD−45°3218	3.18	1.5(19)	4.8(19)	2.7(18)	1.0(18)	2.9(16)	2.7(15)	1.8(13)
CPD−46°3272	3.18	1.7(19)	5.2(19)	2.9(18)	1.1(18)	3.2(16)	2.9(15)	1.9(13)
HD 73882	2.13	1.3(19)	4.0(19)	2.2(18)	8.5(17)	2.4(16)	2.2(15)	1.5(13)
HD 111973	1.00	6.5(18)	2.0(19)	1.1(18)	4.2(17)	1.2(16)	1.1(15)	7.4(12)
HD 111904	1.00	6.5(18)	2.0(19)	1.1(18)	4.2(17)	1.2(16)	1.1(15)	7.4(12)
HD 111934	1.08	6.5(18)	2.0(19)	1.1(18)	4.2(17)	1.2(16)	1.1(15)	7.4(12)
HD 111990	1.16	7.7(18)	2.4(19)	1.3(18)	5.1(17)	1.5(16)	1.3(15)	8.9(12)
CPD−59°4551	1.40	1.4(19)	4.4(19)	2.4(18)	9.3(17)	2.7(16)	2.5(15)	1.6(13)
HD 114886	1.28	1.0(19)	3.2(19)	1.8(18)	6.8(17)	1.9(16)	1.8(15)	1.2(13)
HD 115704	2.22	1.5(19)	4.8(19)	2.7(18)	1.0(18)	2.9(16)	2.7(15)	1.8(13)
HD 112366	2.24	1.2(19)	3.6(19)	2.0(18)	7.6(17)	2.2(16)	2.0(15)	1.3(13)
HD 115363	2.58	9.0(18)	2.8(19)	1.6(18)	5.9(17)	1.7(16)	1.6(15)	1.0(13)
HD 110639	2.74	1.9(19)	6.0(19)	3.3(18)	1.3(18)	3.6(16)	3.3(15)	2.2(13)
HD 114011	2.90	4.3(19)	1.3(20)	7.3(18)	2.8(18)	8.0(16)	7.4(15)	4.9(13)
HD 113432	3.06	1.9(19)	6.0(19)	3.3(18)	1.3(18)	3.6(16)	3.3(15)	2.2(13)
HD 113422	3.24	3.0(19)	9.2(19)	5.1(18)	1.9(18)	5.6(16)	5.1(15)	3.4(13)
HD 112272	3.26	2.1(19)	6.4(19)	3.6(18)	1.4(18)	3.9(16)	3.6(15)	2.4(13)
HD 114213	3.42	6.5(18)	2.0(19)	1.1(18)	4.2(17)	1.2(16)	1.1(15)	7.4(12)

the gas toward HD 62150, HD 75149, and CPD−44°3129. For more reddened sight lines such as toward HD 63804, HD 78344, and HD 75211, $N(C_2)$ and $N(CN)$ are nearly independent of density because production and destruction involve collisions.

We also determined column densities in the $J''=0$–6 rotation levels in $v''=0$ of the electronic ground state of molecular hydrogen. Predicted column densities are given in Table 13 in Cols. 3–9. The syntax x(nn) used in that table describes values of $x\times10^{nn}$. These predictions of H_2 columns from our models can be tested through future FUSE observations. One star, HD 73882, has been observed with FUSE (Snow et al. 2000). The total hot component of H_2 ($J''>1$) found in our model is similar to the observations, although the population density in the highest levels ($J''>4$) is larger than our predictions. The H_2 excitation temperature toward HD 73882 from the MHD model is 200 K, compared to a value of 300 K inferred from the observations. Either the MHD models do not heat the gas sufficiently, or the high-J values are populated primarily by UV pumping from the O8.5 star as claimed by Snow et al. (2000).

5. Summary

We present CN observations for the three southern translucent clouds which obscure stars in the NGC 2439, Vela OB1, and Cen OB1 associations. The CN data complement previous detections of CH, CH^+, and C_2. Altogether, we present a homogeneous set of CH, CH^+, CN, and C_2 column densities and radial velocities. We use

the CN data to study its production via chemical models. Our main results are:

- The observed column densities of CN and C_2 are well reproduced by our chemical reaction network of quiescent molecular gas.
- Most lines of sight through the three translucent clouds test diffuse material, characterised by densities of a few hundred cm^{-3} and ultraviolet radiation fields 1–5 times the average interstellar flux. The densities inferred here from CN are in excellent agreement with previously inferred densities from C_2 excitation.
- The radial velocities of CN agree with those of CH, CH^+, C_2, and CO.
- An additional gas component containing 10–50 MHD shocks in each line of sight explains the observed column densities of CH^+ and 10 to 30% of the observed CH column.

Acknowledgements. SRF was supported in part by NASA LTSA grant NAG5-4957. It is a pleasure to thank the referee, Dr. Steve Fossey, for his thorough review of the paper and his valuable comments to improve the manuscript.

References

Bauschlicher, C. W. Jr., Langhoff, S. R., & Taylor, P. R. 1988, ApJ, 332, 531
Black, J. H., & van Dishoeck, E. F. 1988, ApJ, 331, 986
Black, J. H., & van Dishoeck, E. F. 1991, ApJL, 369, L9
Le Bourlot, J., Pineau des Forêts, G., Roueff, E., & Schilke, P. 1993, ApJ, 416, L87
Bucher, M. E., & Glinski, R. J. 1999, MNRAS, 308, 29
Crane, P., Lambert, D. L., & Sheffer, Y. 1995, ApJS, 99, 107
Crawford, I. 1995, MNRAS, 277, 458
Crawford, I. 1997, MNRAS, 290, 41
Davis, S. P., Shortenhaus, D., Stark, G., et al. 1986, ApJ, 303, 892
Duley, W. W., Hartquist, T. W., Sternberg, A., Wagenblast, R., & Williams, D. A. 1992, MNRAS, 255, 463
Draine, B. T., & Katz, N. 1986, ApJ, 310, 392
Falgarone, E., Pineau des Forets, G., & Roueff, E. 1995, A&A, 300, 870
Federman, S. R., Danks, A. C., & Lambert, D. L. 1984, ApJ, 287, 219
Federman, S. R., & Lambert, D. L. 1988, ApJ, 328, 777
Federman, S. R., Knauth, D. C., Lambert, D. L., & Andersson, B.-G. 1997a, ApJ, 489, 758
Federman, S. R., Strom, C. J., Lambert, D. L., et al. 1994, ApJ, 424, 772
Federman, S. R., Welty, D. E., & Cardelli, J. A. 1997b, ApJ, 481, 795
Fixsen, D. J., Mather, J. C., Shafer, R. A., Brodd, S., & Jensen, K. A. 1997, AAS, 191, 91.05
Flower, D. R., & Pineau des Forêts, G. 1998, MNRAS, 297, 1182
Gredel, R. 1997, A&A, 320, 929, Paper I
Gredel, R. 1999, A&A, 351, 657
Gredel, R., van Dishoeck, E. F., & Black, J. F. 1991, A&A, 251, 625
Gredel, R., van Dishoeck, E. F., & Black, J. F. 1993, A&A, 269, 477
Jenkins, E. B. 1986, ApJ, 304, 739
Joseph, C. L., Snow, T. P., Jr., Seab, C. G., & Crutcher, R. M. 1986, ApJ, 309, 771
Joulain, K., Falgarone, E., Pineau des Forêts, G., & Flower, D. 1998, A&A, 340, 241
Knauth, D. C., Federman, S. R., Pan, K., Yan, M., & Lambert, D. L. 2001, ApJS, 135, 201
Lambert, D. L., Sheffer, Y., & Crane, P. 1990, ApJ, 359, L19
Meyer, D. M. 1997, in Molecules in Astrophysics: Probes and Processes, ed. E. F. van Dishoeck (Kluwer), 407
Meyer, D. M., Cardelli, J. A., & Sofia, U. J. 1997, ApJ, 490, L103
Meyer, D. M., Jura, M., & Cardelli, J. A. 1998, ApJ, 493, 222
Münch, G. 1968, in Nebulae & Interstellar Matter, ed. B. M. Middlehurst, & L. H. Aller (Univ. Chicago Press), 365
Pan, K., Federman, S. R., & Welty, D. E. 2001, ApJ, 558, L105
Pineau des Forêts, G., Flower, D. R., Hartquist, T. W., & Dalgarno, A. 1986, MNRAS, 220, 801
Prasad, C. V. V., Bernath, P. F., Frum, C., & Engleman, R. Jr. 1992, J. Molec. Spec., 151, 459
Reed Cameron, B. 2000, AJ, 119, 1855
Roth, K. C., & Meyer, D. M. 1995, ApJ, 441, 129
Snow, T. P., et al. 2000, ApJ, 538, L65
Sofia, U. J., Cardelli, J. A., Guerin, K. P., & Meyer, D. M. 1997, ApJ, 482, L105
Spaans, M. 1995, Ph.D. Thesis, Models of Inhomogeneous Interstellar Clouds (Leiden)
Strömgren, B. 1948, ApJ, 108, 242
van Dishoeck, E. F., & Black, J. H. 1989, ApJ, 340, 273
Zsargó, J. 2000, Ph.D. Dissertation, Univ. of Toledo